Thesis for The Degree of Licentiate of Engineering

Electrode Degradation in Polymer Electrolyte Fuel Cells

Linnéa Strandberg

CHALMERS
UNIVERSITY OF TECHNOLOGY

Department of Physics
Chalmers University of Technology
Gothenburg, Sweden, 2023

Electrode Degradation in Polymer Electrolyte Fuel Cells

Linnéa Strandberg

© Linnéa Strandberg, 2023

Department of Physics
Division of Chemical Physics
Chalmers University of Technology
SE-412 96 Göteborg,
Sweden
Phone: +46(0)31 772 1000

Cover:
Platinum nanoparticles on carbon support under a microporous layer.

Printed by Chalmers Digitaltryck,
Gothenburg, Sweden 2023.

"If the string brakes, try another piece of string."
- Owl

Electrode Degradation in Polymer Electrolyte Fuel Cells

Linnéa Strandberg

Department of Physics
Chalmers University of Technology

Abstract

To mitigate the climate crisis, and reduce carbon emissions from e.g. the transport and energy sectors, hydrogen has been proposed to be used as an environmentally friendly alternative energy carrier. Proton exchange membrane fuel cells (PEMFCs) use hydrogen as a fuel to create electricity with the only byproducts being water and heat, and are well suited as a power source for e.g. vehicles. However, for successful commercialisation of PEMFCs, some hurdles need to be overcome. In particular, lifetime is a limiting factor for PEMFC due to harsh operational conditions. To improve lifetime, the mechanisms by which the materials in PEMFCs degrade must first be better understood.

In this thesis, I present a study on the behaviour of Pt, which is currently the sate-of-the-art catalyst for PEMFC, during electrochemical procedures in liquid electrolytes, studied using electrochemical quartz crystal micro-balance (EQCM). Mass response and dissolution rates for Pt thin films were studied in acid and alkaline environments. The Pt dissolution rate was found to be similar in alkaline and acidic electrolyte when normalised to electrochemical surface area.

Furthermore, I present identical location (IL) microscopy implemented in a real $5\,\mathrm{cm}^2$ single-cell fuel cell, to follow the degradation of Pt catalyst on carbon support under realistic operation conditions. With both IL scanning electron microscopy (IL-SEM) and IL transmission electron microscopy (IL-TEM), I show that the degradation processes can be followed during different types of ageing processes. IL-SEM show that the carbon support material is stable during normal fuel cell operation conditions, while the Pt particles grow. IL-TEM show similar result for the normal condition operation as seen with the IL-SEM. However, during start-up/shutdown conditions, IL-TEM show that the carbon support lose volume, and collapse on weak points, which brings Pt particles together, and promotes Pt particle growth. The developed IL techniques presented in this thesis helps distinguish the degradation effects of different operation conditions and opens up for further testing of degradation processes under real fuel cell conditions.

Keywords

Fuel cells, Platinum stability, Catalyst degradation

List of Publications

This thesis is based on the following publications:

Paper I

V. Shokhen*, **L. Strandberg***, M. Skoglundh and B. Wickman
"Impact of Accelerated Stress Tests on the Cathodic Catalytic Layer in a Proton Exchange Membrane (PEM) Fuel Cell Studied by Identical Location Scanning Electron Microscopy"
ACS Applied Energy Materials
vol. 5, no. 9, pp. 11200-11212, 2022
* equal contribution

Paper II

L. Strandberg, V. Shokhen, M. Luneau, G. Lindbergh, C. Lagergren and B. Wickman
"Comparison of Oxygen Adsorption and Platinum Dissolution in Acid and Alkaline Solutions Using Electrochemical Quartz Crystal Microbalance"
ChemElectroChem
vol. 9, no. 22, p. e202201030, 2022

Paper III

V. Shokhen*, **L. Strandberg***, M. Skoglundh and B. Wickman
"Fuel Cell Electrode Degradation Followed by Identical Location Transmission Microscopy"
Submitted
2022
* equal contribution

Author Contributions

Paper I
I helped perform measurements, analyse the data, prepare the first draft of manuscript and finalise the manuscript.

Paper II
I designed the experiment, prepared the samples, performed the EQCM measurements and analysed the data. I wrote the first draft of the manuscript and finalised the manuscript.

Paper III
I helped develop the methodology, prepare the samples, perform the measurements, analyse the data, prepare the first draft and finalise the final manuscript.

List of Abbreviations

AEMFC	Anion exchange membrane fuel cell
AFC	Alkaline fuel cell
AST	Accelerated stress test
BEV	Battery electric vehicle
BOL	Beginning of life
BSE	Backscattered electrons
CCM	Catalyst coated membrane
CE	Counter electrode
CL	Catalytic layer
COR	Carbon oxidation reaction
CV	Cyclic voltammentry/voltammogram
E-beam	Electron beam
ECSA	Electrochemical available surface area
EOL	End of life
EQCM	Electrochemical quartz crystal microbalance
FCV	Fuel cell vehicle
GDL	Gas diffusion layer
GHG	Green house gas
HDV	Heavy duty vehicle
HFR	High frequency resistance
HOR	Hydrogen oxidation reaction
IL	Identical location
LDV	Light duty vehicle
MEA	Membrane electrode assembly
MPL	Micro porous layer
OCV	Open circuit voltage
ORR	Oxygen reduction reaction
PEM	Proton exchange membrane
PEMFC	Proton exchange membrane fuel cell
PGM	Platinum group metal
Pt/C	Pt on carbon
QCM	Quartz crystal microbalance
RE	Reference electrode
RH	Relative humidity
RHE	Reversible hydrogen electrode

SE	Secondary electrons
SEM	Scanning electron microscopy
TEM	Transmission electron microscopy
UPL	Upper potential limit
WE	Working electrode

Contents

Abstract iii

List of Publications v

Contributions to Appended Papers vi

List of Abbreviations ix

1 Introduction 1
1.1 Scope of this Thesis 5

2 Catalysis & Electrochemistry 7
2.1 Catalysis 7
2.2 Electrochemistry 10
2.2.1 Redox Reactions 11
2.2.2 Electrocatalysis 13

3 Fuel Cells 15
3.1 Proton Exchange Membrane Fuel Cells 15
3.1.1 Fuel Cell Components 16
3.1.1.1 Catalyst Layers 17
3.1.1.2 Proton Exchange Membrane 19
3.1.1.3 Gas Diffusion Layers 20
3.1.1.4 Flow Fields & Current Collectors 21
3.1.1.5 Humidifiers 22
3.1.1.6 Supporting Hardware 22
3.1.2 Reaction Pathways 23
3.1.3 Figures of Merit 24
3.1.3.1 Efficiency 25
3.1.3.2 Fuel Cell Degradation 28

4 Methods 33
4.1 Electrochemical Measurements 33
4.1.1 Set-ups 33
4.1.1.1 Electrochemical Quartz Crystal Microbalance . 34
4.1.1.2 Fuel Cell Measurements 35

4.1.2 Electrochemical Characterisation 37
4.1.2.1 Cyclic Voltammetry 37
4.1.2.2 Polarisation Curves 39
4.1.2.3 Electrochemical Impedance Spectroscopy . . . 39
4.1.3 Accelerated Stress Tests 39
4.2 Physical Characterisation 41
4.2.1 Electron Microscopy 41
4.2.1.1 Identical Location Micrography 43
4.3 Sample Preparation 43
4.3.1 Thin Film Fabrication 43
4.3.2 Micrography Preparation 44

5 Results **45**
5.1 Mass Response & Dissolution of Pt Thin Films 45
5.2 Accelerated Stress Tests 48
5.2.1 Method Verification 49
5.2.2 Degradation of Performance 49
5.2.3 Particle Growth & Support Degradation 52

6 Conclusions & Outlook **59**

Acknowledgement **61**

Bibliography **63**

Chapter 1

Introduction

The last two centuries have shown a marked improvement in human living standards through the use of technological innovations. Unfortunately, these technological advances have been followed by an increase in greenhouse gas (GHG) emissions (Fig. 1.1), leading us down a path of global warming and extreme weather events [1]. The global average temperature has already risen to 1.1 °C above pre-industrial temperatures [1], which, if no actions are taken, risks continuing to increase to well above the 2 °C target set by the Paris agreement [2].

What measures can and should be taken to reduce GHG emissions, lessen the effects of climate change and ensure good living standards both for the current generation and for the generations to come?

The United Nations established an action plan, Agenda 2030, with 17 goals for sustainable development that outline a path to sustainable development, for both nature and people. Goal number 7 is focused on "[e]nsur[ing] access to affordable, reliable, sustainable and modern energy for all", of which part of the focus is to "increase substantially the share of renewable energy in the global energy mix" [5].

Sweden aims to be at the forefront of renewable energy production, setting and reaching goals well above the minimum requirements for EU's member states, with more than 60% of the energy production coming from renewable resources [6], made possible by good access to hydro- and wind-power, as well as use of biomass cogeneration [7]. With nuclear power included, 98% of Sweden's energy production uses carbon free sources [8]. However, electricity needs to be produced at the moment it is consumed. Even though Sweden have a yearly overproduction of energy, and is a net exporter of electricity [8], the intermittent nature of many renewable energy-sources means Sweden needs to import electricity from neighbour countries that uses e.g. coal and oil when the hydro-plants are drying up or the wind-turbines are not producing enough to satisfy the demand. To fully utilise our resources, and stop our dependence on fossil fuel, energy must somehow be stored during surplus production, to later be used to cover up for our energy consumption during low production.

Apart from the energy sector, another large sector that needs to be decar-

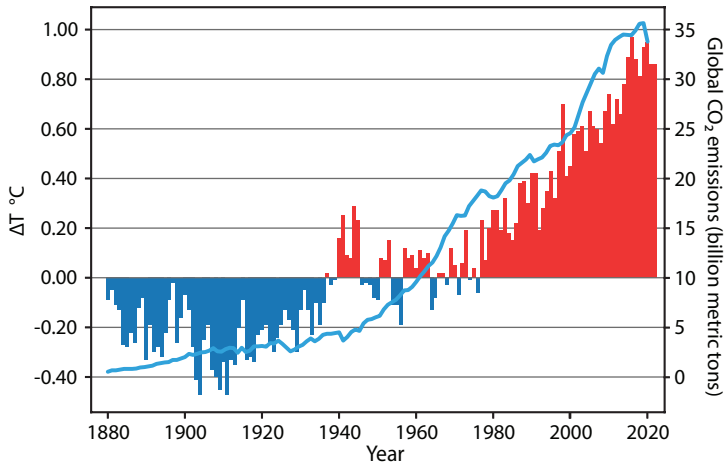

Figure 1.1: Change in average global temperature from 1880 to 2021, compared to the average temperature 1910–2000, and annual global emissions of CO_2. Data from [3, 4]. The data for CO_2 emissions has been converted from metric tons of carbon to metric tons of CO_2 by multiplying it with a factor of 3.664.

bonised is the transport sector. Today, transportation accounts for 16.2% of the total emissions of GHG [9]. To reach net zero emissions, everything from light duty vehicles (LDV) such as small trucks and passenger cars to heavy duty vehicles (HDV) such as long haul transportation and heavy machinery used in industry need alternative energy solutions based on GHG-free technology if the goals of the Paris agreement is to be met. While battery electric vehicles (BEV) have taken a considerable part of the market when it comes to LDV [10], the technology is not optimal for many HDV-applications where aspects such as a large energy capacity, weight limitations, long operation times/ranges and fast refuelling/recharging times are crucial [11, 12].

Hydrogen could be one part of the solution to reduce GHG emissions. Hydrogen, which is the most abundant element in the universe, can be found and extracted from many sources on earth. Depending on the source of hydrogen, and what methods are used to refine it, hydrogen can be classified as either grey, blue or green. Grey hydrogen is produced using hydrocarbon reforming, often with methane as feedstock, in a process known as steam reforming. Globally, 76% of H_2 production comes from steam reforming [13]. In steam reforming, methane is mixed with water in the form of steam, and a mix of hydrogen with small amounts of CO is created over a catalyst [14],

$$CH_4 + H_2O \leftrightarrow CO + 3H_2, \tag{1.1}$$

$$CO + H_2O \leftrightarrow CO_2 + H_2. \tag{1.2}$$

This gas mix is also known as syngas.

CO_2 is produced during the steam reforming process, and if no further steps are taken to hinder CO_2 emission into the atmosphere. If steam reforming is

combined with carbon capture and storage techniques, thus reducing the CO_2 emissions during production, the produced hydrogen is called blue hydrogen instead.

Green hydrogen is hydrogen produced using electrolysis. In electrolysis, electricity is used to split up water into its constituents hydrogen and oxygen,

$$H_2O \rightarrow H_2 + {}^1\!/_2 O_2. \tag{1.3}$$

If the electricity used for this process comes from renewable energy sources such as wind, hydro or solar energy, green hydrogen causes no GHG emissions. Green hydrogen also has a high purity, which is important in many applications sensitive to e.g CO poisoning. Unfortunately, green hydrogen only stand for about 2% of the global hydrogen production [13].

Green hydrogen can be used to help balance an energy system based on renewable sources [13]. During excess production, electrolysers can quickly be started up to produce hydrogen, which can then be stored e.g. in form of liquid hydrogen or as pressurised gas. The hydrogen can later be converted back to electricity when energy production is low, thus balancing the intermittent supply of energy in the power grid, using fuel cells. A fuel cell works like an electrolyser in reverse, combining hydrogen with oxygen to produce water,

$$H_2 + {}^1\!/_2 O_2 \rightarrow H_2O. \tag{1.4}$$

This process releases energy that can be collected in form of electricity, with the only byproducts being pure water and some heat, with no adverse environmental impact. By using electrolysers powered by renewable resources together with fuel cells, hydrogen can become an important energy vector in a GHG free energy system [15–17], see Fig. 1.2.

Apart from having the possibility of being a GHG free energy carrier, hydrogen has several other advantages and benefits. For one thing, the resources needed for green hydrogen production—water—is readily available, and thus hydrogen can be produced locally where it is needed, which could reduce many nations dependency of importing oil and gas from possibly hostile nations. The technology is also very versatile and adaptable. Hydrogen can be produced and used in everything from large scale power plants to small scale domestic appliances. Fuel cells also has the advantage that the power and storage capacity is decoupled, and not directly coupled as it is in batteries.

Hydrogen solutions such as fuel cell vehicles (FCVs) are often compared to battery based solutions such as BEVs, as both are GHG free alternatives to conventional vehicles that uses combustion engines. Among the advantages of FCVs over BEVs is a very high energy density per mass of hydrogen compared to e.g. lithium. As a comparison, hydrogen has a specific energy, energy per mass, of almost 120 MJ/kg, while diesel and gasoline has about a third of that at ca 45 MJ/kg, and batteries only have an energy capacity of 0.1–2 MJ/kg [18]. FCV have operating ranges comparable to those of conventional vehicles, and a much faster refuelling time than BEV, on the orders of minutes in stead of hours, which is a considerable advantage, especially in long haul trucking or

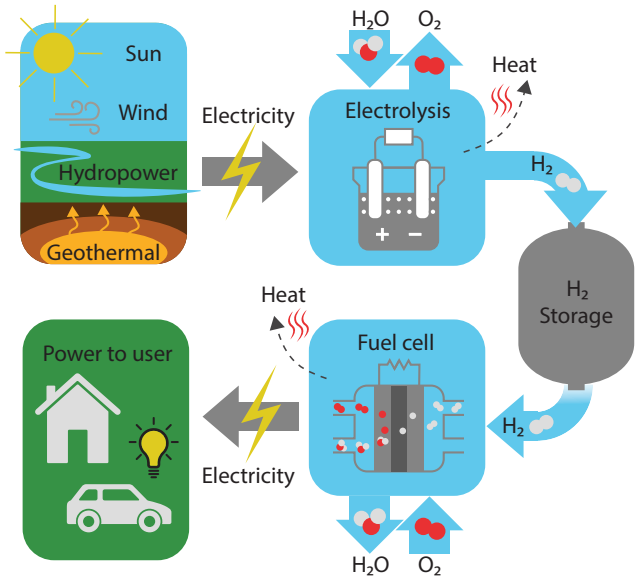

Figure 1.2: Schematic of a GHG free energy system utilising hydrogen as an energy vector.

heavy machinery that needs to be operated continuously in shifts. At shorter distances, BEV are still at an advantage over FCV, for instance in terms of cost. However, in e.g. heavy duty machinery and long distance transportation, FCV are expected to be a good competitor. Nonetheless, fuel cells are an immature technology compared to battery technologies, still mostly used in niche market tests. Furthermore, large scale implementation of FCV requires a build up of infrastructure of the hydrogen supply chain, and a large increase of production capability of hydrogen to meet to expected increase of demand.

Some of the largest barriers for fuel cells today are considered to be cost of production and lifetime [19]. Much of the production cost of a fuel cell stack comes from the need to use expensive raw materials. For a fuel cell to work efficiently, they need catalysts that enable the chemical reactions to occur at a reasonable rate. Due to the harsh conditions of a fuel cell, such as highly acidic environments, and high and varying potentials, platinum or other platinum group metals (PGMs) is the state-of-the-art catalyst for fuel cells. While Pt has a good performance, it is expensive and scarce. At high volume production (>500 000 units/year), up to 40% of the production cost is estimated to come from the use of Pt (Fig. 1.3) [19, 20].

The United States Department of Energy has set several targets for fuel cells to be reached by 2025, such as an 8 000 h lifetime for LDV, a target cost of 30 \$/kW and a loading of 0.10 g_{PGM}/kW [19, 21]. The European initiative Clean Hydrogen Joint Undertaking has adopted similar targets, with the aim

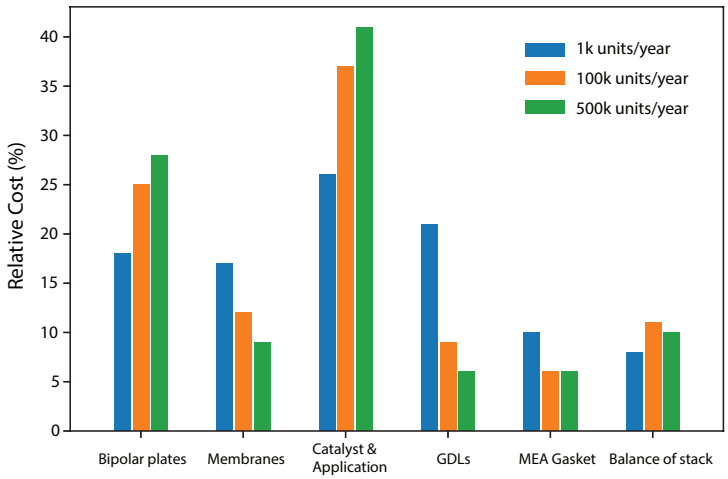

Figure 1.3: Estimated relative cost of proton exchange membrane fuel cell components per yearly production volume. Data from [20].

of achieving lifetimes of 20 000 h by 2024 and 30 000 h by 2030 for HDV [22]. While getting closer to those targets, more development is still needed to successfully introduce fuel cells to the market. To reduce the production cost, effort have been put on either maximising material usage e.g. by the use of nanostructured materials, or to reduce PGM loading by using alloys of PGM with transition metals or rare earth metals. Furthermore, research needs to be done on the degradation mechanisms of fuel cell components, so that more durable materials and better driving routines can be developed to achieve longer lifespans.

1.1 Scope of this Thesis

This thesis aims to contribute to the development of fuel cell technologies for a sustainable and GHG emission free society, by providing insight in how fuel cells, and in particular the Pt catalyst and carbon support in proton exchange membrane fuel cells, degrade during different operational conditions.

In Chapter 2, I present the basics of catalysis and electrochemistry, to provide a background on which further discussion is based. Chapter 3 goes through the theory and construction of proton exchange membrane fuel cells, and different challenges and limitations associated with the components. Chapter 4 describes the most important methods used in the papers included in this thesis, and Chapter 5 summarises some of the results from **Paper I**, **II** and **III**, and, lastly, Chapter 6 summarises the conclusions of this thesis and propose recommendations for further work.

Chapter 2

Catalysis & Electrochemistry

Before delving into the subject of fuel cell systems, first I will go through some of the theory of catalysis and electrochemistry, both of which are fundamental for understanding the principles of fuel cells.

2.1 Catalysis

Catalysis is the act of increasing or modifying the rate of a chemical reaction by the addition of a substance, called catalyst, without the catalyst itself being consumed in the process. Catalysis is immensely important for our society. An estimated 90% of all industry chemicals are produced using catalysis somewhere during the production process [23], such as fertilisers [24], petroleum cracking products [25], polymers [26, 27] and hydrogen from steam reforming [28, 29]. Catalysis is also used for exhaust cleaning [30–33]. Every modern petrol and diesel fuelled car has an exhaust gas catalyst to reduce the amount of harmful and toxic emissions such as NO_x, CO and hydrocarbons emitted during the combustion process.

While only thermodynamically favourable reactions can be catalysed, the addition of a catalyst can drastically increase the reaction rates—often by many orders of magnitudes—thus increasing output. Furthermore, in reactions with several possible products, adding a well chosen catalyst can increase the selectivity, and thus change the ratio between sought after end product and unwanted byproducts.

Catalysis can be divided into two main categories: Homogeneous and heterogeneous. In homogeneous catalysis, the catalyst and the reactants are in the same phase, such as liquid or gaseous, while in heterogeneous catalysis, the catalyst is in a different phase than the reactants. In heterogeneous catalysis, the catalyst is often in a solid phase while the reactants are in a liquid or gaseous phase. The reactions will then take place on the interface between the catalyst surface and the gas/liquid phase.

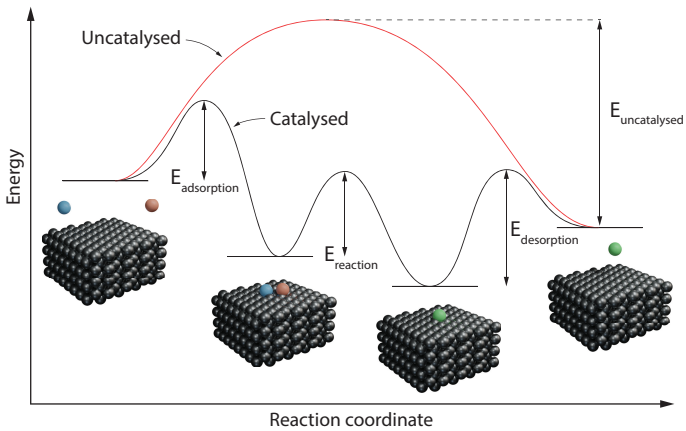

Figure 2.1: Energy diagram of a reaction with and without a catalyst present. The catalyst stabilises intermediate species thus providing an alternative pathway with lower energy barriers.

Fig. 2.1 illustrates the energy diagram of a chemical reaction with and without a catalyst present. The catalyst can stabilise intermediate species, thus providing alternative pathways with lower energy barriers than the uncatalysed reaction. It is important to note that the energy state of the reactants and products will be the same, and that catalysis cannot shift the overall thermodynamics.

The catalysed reaction can generally be divided into a sequence of elementary steps. First, the reactants diffuse to the surface of the catalyst, and adsorb. Then, the reactants undergo reactions on the surface, sometimes through several intermediate steps. Lastly, the products desorb from the surface, and diffuse away. Each elementary step has its own associated energy barrier, and the largest activation barrier will affect the overall reaction rate.

A good tool for screening potential new catalysts is the Sabatier principle. It states that the reactant should bind neither too strongly nor too weakly to the catalyst [34]. If the reactants bind too strongly to the surface, the reactants will not desorb from the surface, physically block further reactants to bind to the surface, and the desorption of products will be the rate limiting step. On the other hand, if the binding strength between reactants and catalyst is too weak, the reactants will not interact with the surface enough, and the adsorption of reactants will be the rate limiting step. The Sabatier principle is illustrated well with a so called Volcano plot. Fig. 2.2 shows the activity of different metals for the oxygen reduction reaction (ORR) as a function of the binding strength between oxygen and the catalyst. The activity follows a volcano shaped pattern. The top of the volcano gives the optimal binding energy, and the activity quickly goes down on either side when deviating from this value.

Apart from the binding energy of reactants and products, the mass activity of a catalyst, number of reactions per mass per time unit, is, among other

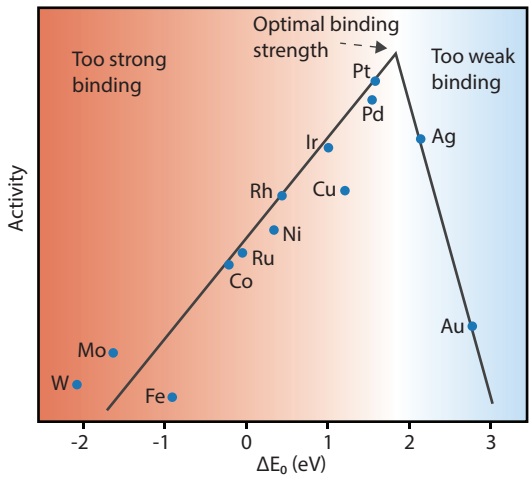

Figure 2.2: Volcano plot of activity vs. oxygen binding energy for the ORR on different metals. Pt is located c.a. 0.1 eV below the optimal binding energy. Data from [35].

things, limited by the available active sites on the surface. To fully utilise all catalyst material, the mass to surface ration should be maximised, which can be accomplished by using nanoparticles or otherwise nanostructured materials.

2.2 Electrochemistry

Electrochemistry, a branch of physical chemistry that deals with the relation between electrical potential and chemical reactions, and the conversion between electrical and chemical energy, has a long history stretching back to the 18^{th} century. In the later end of the 1780s, Luigi Galvani discovered bioelectricity, when he found that the muscles of a dead frog twitched when they were connected to two pieces of metal in a circuit [36]. From this, Galvani concluded that living beings had an innate vital force that he named 'animal electricity'. Galvanis fellow scientific college Alessandro Volta rebutted this idea, and realised that the electricity came not from the frog legs, but from the two different metals in connection with each-other. Volta built further on those ideas, demonstrating in 1794 that an electric current is produced when two sheets of metals and brine-soaked cardboard or cloth is arranged in a circuit [37]. This came to be the *voltaic pile*, which was the first electrical battery. The Voltaic pile was later used by William Nicholson and Anthony Carlisle to discover *electrolysis* of water, where an electrical potential is used to drive the non-spontaneous process of splitting water into hydrogen and oxygen, by connecting a Voltaic pile to a water filled tube via two platinum wires, at which they noticed that bubbles were formed on either wire [38].

The opposite reaction of water electrolysis, producing electricity by combining hydrogen and oxygen, was first demonstrated in 1838 by Sir William Robert Grove, who created a crude version of a fuel cell using sheet iron, copper, porous porcelain plates and a solution of copper sulphate in diluted acid [39]. Despite its early start, it would be almost a century until a practical version of a hydrogen fuel cell was developed, when Francis Thomas Bacon created a 5 kW alkaline fuel cell (AFC) in 1932. The AFC technology was used to generate both power and drinking water for the astronauts in the Apollo program by NASA in the 1960s [40]. The AFC has later been replaced by proton exchange membrane fuel cells (PEMFC), which today is the leading fuel cell technology, although alternatives such as anion exchange membrane fuel cell (AEMFC) are also being researched.

Today, electrochemistry plays a vital roll in many aspects of our life and society, in everything from the batteries in our cell phones, to large scale industrial production of many indispensable chemicals. Together with the rise of electrification within our energy systems, and the shift away from fossil fuels as energy carriers, the importance of electrochemical solutions like batteries and fuel cells cannot be understated.

The basic principle of any electrochemical reaction is the passing of electrons between ions, and these reactions often takes place in the interface between an electrode, which is an electrically conductive material, and an electrolyte, which contains ions. These reactions can either be spontaneous processes, where chemical energy is converted to electrical energy in a galvanic cell, or non-spontaneous reactions where externally provided electrical energy is used to drive chemical reactions in an electrolytic cell.

2.2.1 Redox Reactions

A redox reaction is a chemical reaction where electrons are transferred from one species to another. Every electrochemical reaction is also a redox reaction. A redox reaction can be separated into its two half reactions, which can be separated in space and studied independently. In its simplest form, oxidising species Ox is accepting n electrons to be reduced to Red

$$Ox + ne^- \leftrightarrow Red. \tag{2.1}$$

The quotient Q is the ratio between the activity a of the reduced species and the oxidised species and can, if the activities are close to unity, be approximated by the quotient between the molar concentration of respective species:

$$Q_r = \frac{a_{\mathrm{Red}}}{a_{\mathrm{Ox}}} = \frac{[Red]}{[Ox]}, \tag{2.2}$$

where [ ] is used to denote concentration. Thermodynamics gives us that Gibbs free energy ΔG is related to the Gibbs free energy under standard conditions ΔG^{Θ} by

$$\Delta G = \Delta G^{\Theta} + RT \ln Q_r. \tag{2.3}$$

A redox reaction can be classified as either spontaneous, if the change in Gibbs free energy ΔG is negative, i.e. energy is expelled, or non-spontaneous if ΔG is positive, i.e. energy has to be added for the reaction to occur. ΔG is the maximum amount of work that can be recovered from the reaction. The electrical work performed by a cell is

$$W_{\mathrm{electrical}} = -nFE, \tag{2.4}$$

where F is Faraday's constant, E is the cell potential, and n is the number of electrons exchanged in the process. If all work is converted to electrical work, then it follows that

$$\Delta G = -nFE. \tag{2.5}$$

Combining Eq. 2.3 with Eq. 2.5 gives Nernsts equation for the cell potential

$$E_{\mathrm{Cell}} = E^{\Theta}_{\mathrm{Cell}} - \frac{RT}{nF} \ln Q = E^{\Theta}_{\mathrm{Cell}} - \frac{RT}{nF} \ln \frac{[Red]}{[Ox]}, \tag{2.6}$$

where $E^{\Theta}_{\mathrm{Cell}}$ is the cell potential under standard conditions, which gives the theoretical equilibrium cell voltage when no net current is flowing through the electrode.

When the voltage deviates from the equilibrium potential, current will start to flow through the electrode. The Butler-Volmer equation,

$$j = j_0 \left(\mathrm{e}^{\frac{(1-\alpha)nF\eta}{RT}} - \mathrm{e}^{\frac{-\alpha nF\eta}{RT}} \right), \tag{2.7}$$

where j_0 is the exchange current density, n is the number of electrons transferred in the reaction, and α is a transfer coefficient, describes how the current density j through an electrode relates to the overpotential η, which is a measurement of how much the potential deviates from the equilibrium potential ($\eta = E - E_0$) [41]. At high overpotentials, $|\eta| \gg 0$, one term in Eq. 2.7 goes to zero, and can be neglected. This leads to two different cases depending on if $\eta \gg 0$ or $\eta \ll 0$, representing anodic and cathodic currents, respectively

$$\text{Anodic :} \qquad j = j_0 \mathrm{e}^{\frac{(1-\alpha)nF\eta}{RT}} \tag{2.8}$$

$$\text{Cathodic :} \qquad j = -j_0 \mathrm{e}^{\frac{-\alpha nF\eta}{RT}}, \tag{2.9}$$

Taking the common logarithm of Eq. 2.8 and Eq. 2.9 gives

$$\text{Anodic :} \qquad \log j = \log j_0 + \frac{(1-\alpha)nF\eta}{2.303RT} \tag{2.10}$$

$$\text{Cathodic :} \qquad \log |j| = \log j_0 - \frac{\alpha nF\eta}{2.303RT}. \tag{2.11}$$

Rewriting Eq. 2.10 and 2.11 gives the Tafel equation

$$\text{Anodic :} \qquad \eta = \frac{2.303RT}{\alpha nF} \log j_0 + \frac{2.303RT}{(1-\alpha)nF} \log j \tag{2.12}$$

$$\text{Cathodic :} \qquad \eta = \frac{2.303RT}{(1-\alpha)nF} \log j_0 - \frac{2.303RT}{\alpha nF} \log |j| \tag{2.13}$$

or, in its simplified form,

$$\eta = a + b \log |j|, \tag{2.14}$$

where b is called the Tafel slope. The Tafel slope is found by plotting η vs $\log j$ (Fig. 2.3), and taking the slope of the curve in the linear Tafel region. The transfer coefficient α can be calculated from the Tafel slope, and the exchange current density j_0 is found by extrapolating the line and finding the intersection with the x-axis.

Pourbaix diagrams show the pH dependence for the potential of different reactions, and shows which species is stable at respective potential. For H_2O at pH 0, the Pourbaix diagram shows that the window of stability is between 0 and 1.23 V, see Fig. 2.4a. At 1.23 V and above, water is evolved into O_2(g), and below 0.0 V water is evolved into H_2(g). At higher pH, these potential limits shift, according to

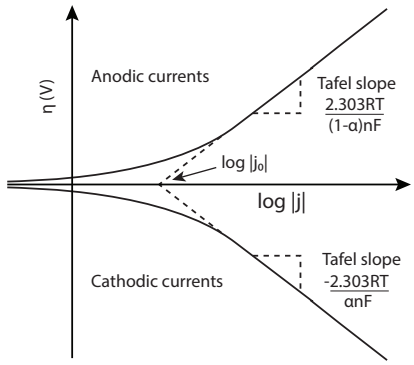

Figure 2.3: Tafel plot showing anodic and cathodic currents for $\alpha = 0.5$. The Tafel slope is taken from the linear portion of the plot, and the exchange current j_0 is found at the intersection of the slope with the x-axis.

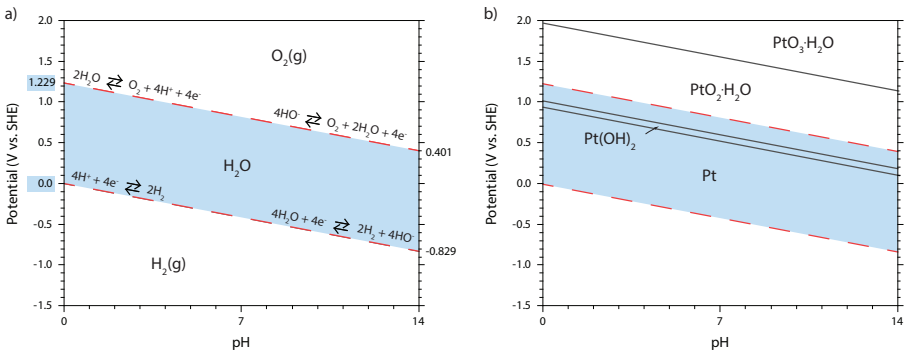

Figure 2.4: Pourbaix diagram, showing the the thermodynamically stable phases for different potentials at a specific pH, of a) water and b) Pt. The blue area shows the stability domain for water which at pH 0 is 0–1.23 V. Data from [42].

$$E = E_0 - \text{pH} \times \frac{2.303RT}{F}, \tag{2.15}$$

where E_0 is the redox potential at pH 0, R is the gas constant, T is the temperature, F is the Faraday constant and $2.303RT/F \approx 59$ mV at 25 °C. However, the potential difference between oxygen evolution and hydrogen evolution for any given pH will still be 1.23 V.

2.2.2 Electrocatalysis

Electrocatalysis is a subset of catalysis that deals with catalysis of electrochemical reactions. In an electrochemical set-up, the electrocatalyst is either the electrode itself, such as copper plates, or supported on the electrode, e.g.

in form of nanoparticles. The electrocatalyst works by changing activation overpotentials, thereby changing the potential at which a specific reaction occurs. In a Galvanic cell, i.e. a cell where the reactions are spontaneous, the overpotential determines how much voltage is lost compared to the theoretical maximum, while in an electrolytic cell, i.e. a cell where external energy input is required to drive the cell, the overpotential of the cell determines how much more energy is needed to drive the reaction. In both cases, overpotentials leads to loss of efficiency and the potentially useful energy is lost as heat. Thus one criteria for good electrocatalyst is to have high current densities at low overpotentials, also known as activity. Some other key criteria for an efficient electrocatalyst includes selectivity and stability. Stability of the electrocatalyst means it should be able to withstand the relevant potential ranges and operational conditions, with as little degradation and deactivation as possible.

Chapter 3

Fuel Cells

A fuel cell is, much like a battery, a galvanic cell where energy stored in chemical bonds are converted to electrical energy through a pair of redox reactions. However, unlike a battery, where a limited amount of the chemical reactants are stored internally, the fuel of a fuel cell is provided externally, and they can thus keep producing electricity for as long as fuel and oxidants are provided.

There are many different types of fuel cells, that are often divided into groups depending on which type of electrolyte or fuel they use, and at which temperature they operate. However, the basic structure and concept is the same for all types of fuel cells: An anode, where a chemical is oxidised, and a cathode, where a chemical is undergoing reduction, are connected via an electrolyte, either in liquid or solid form, which allows for ions to be conducted between the two reaction sites. Fuel and oxidants in gas or liquid form are supplied continuously to either electrode respectively.

One of the more commercially successful types of fuel cells are PEMFCs, which are acidic in their nature due to utilising protons as charge carriers. The anion exchange membrane fuel cells are the analogous technology based on alkaline membranes. The focus in this thesis will be on on PEMFC. However, AEMFCs are based on similar principles.

3.1 Proton Exchange Membrane Fuel Cells

PEMFCs are one of the more well-researched and used type of fuel cell. PEMFCs operate at around 80 °C and are classified as low temperature fuel cells, as compared to e.g. solid oxide fuel cells which can operate at over 750 °C [43]. A PEMFC uses hydrogen as a fuel and combine it with oxygen, often provided from the air, in an exothermic reaction to create water,

$$\mathrm{H_2} + {}^1\!/_2\ \mathrm{O_2} \rightarrow \mathrm{H_2O}, \tag{3.1}$$

and thus, the only byproducts in this reaction are pure water and heat. To make use of the energy released during Eq. 3.1, the reaction is separated into

its two half reaction. At the anode, hydrogen is split up into protons and electrons in the hydrogen oxidation reaction (HOR),

$$H_2 \rightarrow 2H^+ + 2e^- \qquad E = 0.0\ V_{RHE}, \tag{3.2}$$

where RHE stands for the reversible hydrogen electrode, and at the cathode, the protons and electrons is combined with oxygen to form water, in the ORR,

$$2H^+ + 2e^- + 1/2\ O_2 \rightarrow H_2O \qquad E = 1.23\ V_{RHE}. \tag{3.3}$$

3.1.1 Fuel Cell Components

The two half reactions in Eq. 3.2 and Eq. 3.3 are separated in space, with protons flowing between the half reaction via a separating electrolyte membrane while electrons have to flow through an external circuit, thus providing electrical energy. To achieve this, the fuel cell is designed in a sandwich-like structure (see Fig. 3.1), consisting of current collectors, gas flow fields, gas diffusion layers, catalyst layers, an ion conducting layer, and supporting hardware and software like gaskets, end plates and control systems.

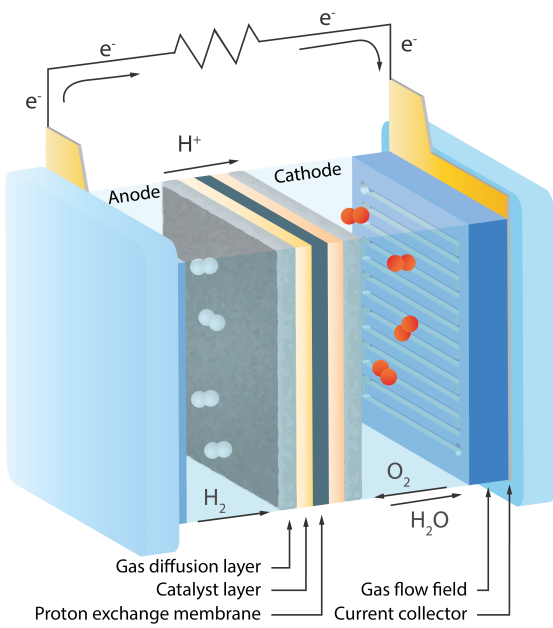

Figure 3.1: Schematic illustration of a single cell proton exchange membrane fuel cell.

3.1.1.1 Catalyst Layers

The actual chemical reactions in the PEMFC take place on the catalyst layers (CLs). The major role of the CLs is to provide a large amount of active sites per geometric surface area of the fuel cell, to facilitate large enough current densities. Today, the state of the art catalyst for both the anodic and the cathodic side of PEMFCs is Pt nanoparticles on carbon support (Pt/C) [44]. Typically, very fine Pt particles are dispersed on supporting carbon particles 3.2. The size of the Pt particles is a trade-off between stability and activity. Smaller particles allows for a higher utilisation Pt due to a larger surface area and thus a higher mass activity, however, smaller particles are unstable and suffers greatly from degradation and dissolution. Larger Pt particles are more stable but have a smaller mass activity. It has been suggested that the optimal Pt particle size is around 2–5 nm [45, 46].

The carbon support, often carbon black, should have a high surface to volume ration, to allow for a high loading of Pt per electrode surface area. For example, KetjenBlack Carbon Black has a surface area of over 1200 m^2 g^{-1} [47]. The carbon black is made up of primary particles ca 30–50 nm in diameter, that forms aggregates. These aggregates forms even larger agglomerates, creating a highly porous structure that allows for gases to reach the reaction sites on the Pt particles. Furthermore, the carbon is a good electrical conductor, providing or removing electrons to the reaction sites as needed.

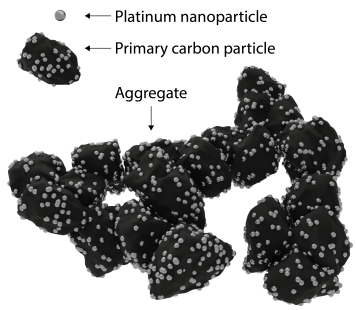

Figure 3.2: Illustration of carbon supported platinum catalyst particles. Pt nanoparticles are dispersed on the surface of primary carbon particles, which forms aggregates together that creates a porous structure.

To provide protons to the reaction sites, the Pt/C is covered with ionomer, a type of polymers with ion conducting properties. While the ionomer is vital for providing protons to the reaction site, it also blocks access for the oxygen, thus a compromise between proton conductivity and fuel access has to be reached when deciding the ionomer loading of the catalyst [48, 49].

The catalysed reactions can occur only if oxygen, electrons and protons are present. This happens on sites where pores for gas transport, carbon support for electrical conduction and ionomer for proton conduction meet. These sites are of utmost importance for the fuel cell, and are often referred to as the triple phase boundary (TPB). Fig. 3.3 shows an illustration of the TPB in the Pt/C.

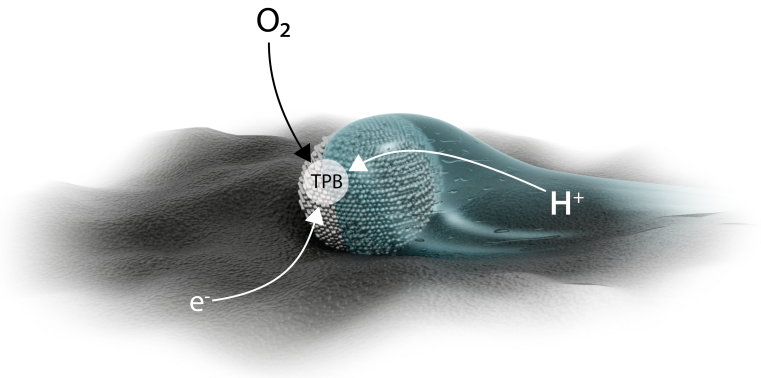

Figure 3.3: Illustration of the triple phase boundary where the electron conductor (carbon support), the ion conductor (ionomer) and the 'porous' gas phase meet on the catalyst.

Pt is the industry standard today due to its good activity towards both the ORR and HOR. Why that is the case becomes clear when looking at the binding energy between Pt and the intermediate species of the reactions, which shows that the binding energy of Pt is just 0.1 eV to low, putting it close to the optimal value, as seen in Fig. 2.2b [35]. Even so, much effort in fuel cell research focuses on finding alternative catalyst materials. Pt is an expensive metal, and in large scale production, the raw cost of Pt can stand for up to 40% of the production cost [19]. And even though Pt has a high activity for both the HOR and the ORR and relatively good stability in the harsh conditions of the fuel cell [44, 50], the highly corrosive environment in the PEMFC means even Pt suffers from degradation [46]. It is hard to find a suitable replacement for Pt that is both more affordable, but also has a high activity and is stable in the highly corrosive environments and shifting potentials of a PEMFC.

Much efforts in reducing the Pt load is focused on either alloying or doping Pt with e.g. transition metals, and/or to create nano-structured Pt particles in an effort to maximise the active sites. For example, suggested Pt alloys include Ni, Cr, Fe and Co [35] and Pt with rare earth metals such as scandium, hafnium and yttrium, the last of which which have been shown to increase the activity up to 9 times [51–54]. Pt particles with well controlled facets such as octahedrons and shape and structure controlled Pt/Pt-alloys such as core-shell particles and nanoframes have been produced showing increased activities compared to common Pt [55–59]. However, while many novel catalyst show highly promising results in laboratory settings, these results are often hard to upscale.

3.1.1.2 Proton Exchange Membrane

An important part of the fuel cell is the proton exchange membrane (PEM), also known as polymer electrolyte membrane. The PEM is located between the anodic and the cathodic CL, physically separating them, and these three components together form what is known as the catalyst coated membrane (CCM). As the name implies, the primary function of a PEM is to act as a solid electrolyte, conducting protons between the anode and the cathode reactions. Moreover, the PEM acts as a physical barrier that prevents hydrogen and oxygen to crossover from their respective side, and reacting directly with each other which would lead to losses of useful fuel. The PEM also needs to be electrically insulating to prevent short circuits, as well as be able to tolerate the harsh environments of the fuel cell. Thus, a good PEM needs high proton conductivity, low gas permeability, high electrical resistance, and high thermal and chemical stability [60, 61].

The membranes are made of ionomers, the same material used to provide proton conductivity to the CLs. Today, the state of the art ionomer used in PEMFCs is Nafion, a sulfonated tetrafluoroethylene based fluoropolymer-copolymer (Fig. 3.4) that was first synthesised by Walther Grot in the 1960s [62]. The backbone of Nafion is polytetrafluoroethylene, more commonly known as PTFE, which has good chemical resistance thanks to the strong bond between carbon and fluorine atoms. PTFE is also highly hydrophobic, which is favourable for removing water out of the membrane. For ion conductivity, sulfonic side chains, SO_3^- are added to the backbone. These sulfonic groups attract H^+ ions, and are very hydrophilic. The sulfonic groups attracts water creating water clusters inside the Nafion, which means that Nafion can adsorb up to 50% of its dry weight in water [60, 63]. At these hydrated regions, the bond between H^+ ions and the SO_3^- groups is weak, and the H^+ ions are mobile. Furthermore, it has been shown that the H^+ ions can move through the so called Grotthuss mechanism, where the ions can 'jump' between water molecules [64]. Thus, when Nafion is hydrated has good conductive properties [63].

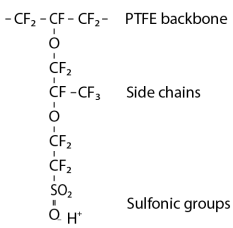

Figure 3.4: Chemical structure of Nafion.

While Nafion is the leading ionomer for membranes today, and have a reasonable tolerance to the current operational conditions, ongoing endeavours to increase the operating temperature of PEMFC leads to a need to develop new alternatives [65–67]. Currently PEMFCs are operated at around 80 °C. However, to improve the kinetics, help with water management to prevent

flooding, reduce the need for cooling systems and increase CO-poisoning tolerance, efforts are currently being made to increase the operating temperature to 100 °C or above [60, 65, 68, 69]. Nafion is highly hydrophobic, and requires high hydration to maintain its proton conducting properties. At high operating temperatures, Nafion can dry out quickly which causes its ion conductive capabilities decreases by several orders of magnitude [60, 66, 67]. Some of the issues with losing water through evaporation can be avoided by operating the fuel cell at elevated pressures, but then power needs to be used to compress the gases. Furthermore, Nafion has a glass transition temperature of around 120 °C [70], and its side-chains start to change structure and relax at around 100 °C [71], which can lead to issues with stability and durability if the membrane is operated at elevated temperatures.

Another important aspect of the PEM is the thickness. To maximise the overall fuel cell volume to power ratio, and improve ion conductivity, the PEM would benefit from being thinner. However, the thinner the membrane is, the more gas crossover will occur [72, 73]. Especially hydrogen is hard to prevent from permeating through the membrane due to it being the smallest and lightest of all elements. Such gas crossover leads to potential losses, and increase degradation of the PEM. Furthermore, the membrane needs to have good mechanical stability. When designing the membrane, the thickness have to be a compromise between these requirements.

3.1.1.3 Gas Diffusion Layers

The main purpose of the gas diffusion layers (GDLs) is to transport reactive gases to the CLs in the fuel cell. However, the GDL has additional important functions. The GDL should remove excess water to prevent flooding, provide electrical contact with the external circuit and provide some mechanical stability [74–76]. To achieve this, the GDL are constructed out of porous conductive materials such as carbon. Commonly either carbon paper—non-woven carbon fibres pressed to a sheet—or carbon cloth is used, and the thickness of the GDL is typically in the range of 100–400 µm [74–77]. Fig. 3.5 shows a typical GDL made of carbon paper. Carbon based GDLs are preferred for their good electrical conductivity, durability and gas permeability. The GDL is often coated with a microporous layer (MPL), a layer of carbon black treated with PTFE. The hydrophobic nature of the MPL facilitates water removal, and the microscopic structure improves electrical contact between the CL and the MPL and helps distribute the gases evenly over the CL [74, 77]. Careful water management is of utmost important to the function of the MEA. If the membrane becomes too dry, the proton conductivity will suffer and the membrane risk degrading, while too much water will cause flooding and block pores, leading to gas transport limitations [74].

The GDLs are mounted on either side of the CCM, with the MPLs facing the CLs, together with supporting gaskets, to form the membrane electrode assembly (MEA) (Fig. 3.6a). Ambiguity can sometimes arise from the terminology, since the CCM is also sometimes referred to as an MEA. To distinguish between the two, they are sometimes referred to as 3-layer MEA or a 5-layer

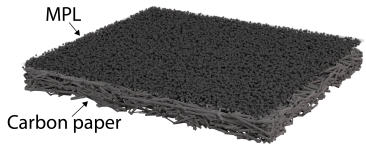

Figure 3.5: Gas diffusion layer made out of carbon fibre paper with a microporous layer.

MEA, for the CCM and the full MEA with GDL, respectively. An alternative approach to construct an MEA is to deposit the CL directly onto the GDL, and then press two GDLs together with a separating membrane.

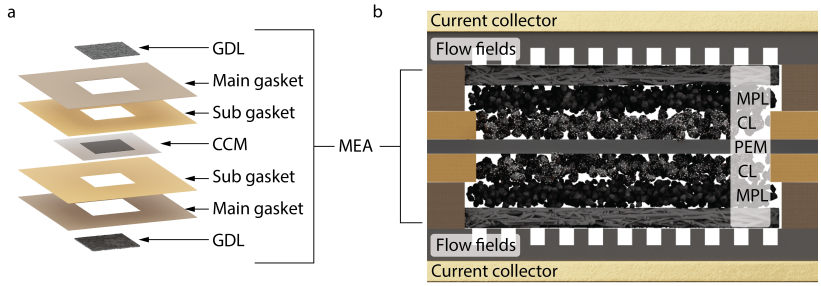

Figure 3.6: a) Construction of an MEA. One GDL is placed on either side of a CCM, with the MPL facing the CL. The assembly is held in place with the help of gaskets, that also serves to seal in the gases. b) Cross-section of an assembled single cell fuel cell.

3.1.1.4 Flow Fields & Current Collectors

Part of the supporting structures include the flow fields and the current collectors. The flow fields are placed next to the GDLs, and serve to distribute fuel to the anode and cathode and to provide electrical contact between the MEA and the current collectors which are placed outside the flow fields, see Fig. 3.5b. The physical distribution of gases is achieved by well designed flow field patterns, in which the gases can flow. Some of the common flow field patterns include serpentine fields, parallel channels and grid type patters, all of which have slightly different properties when it comes to fuel distribution [78, 79]. Furthermore, the flow-fields must be electrically conductive, allow for heat transport, be chemically and mechanically stable, be gas tight, have low weight and volume, and be easily manufacturable [79, 80]. The flow fields are commonly made out of graphite, or stainless steel. While stainless steel plates have good conductive properties and can easily be made thin, they tend to corrode and have a high density, making for heavier systems. Graphite on the other hand is much lighter, but are more brittle and needs to be made ticker to have adequate mechanical durability. The flow fields are in contact with the current collectors, to which the external circuit is connected.

To achieve higher voltages than can be achieved in one single fuel cell, fuel cell stacks are used. In a fuel cell stack, several single cell fuel cell assemblies (each composed of their own MEA) are stacked together end to end where the anode of one cell is connected to the cathode of the next, with separating plates serving as flow fields for both ends in-between. These plates are known as bipolar plates.

3.1.1.5 Humidifiers

The performance of the PEMFC is strongly related to the humidity levels in the cell [81, 82]. The water in the system helps with proton conduction through the membrane channels and the ionomer, and with transferring protons to platinum that is not in sufficient contact with the ionomer. While water is generated in the cell during operation at the cathode, the water evaporation due to the elevated temperature, and the tendency for protons to drag water with them while wandering through the membrane from the anode to the cathode due to electro-osmotic, drag means that especially the anode tend to be susceptible to drying out [61, 83]. To keep the humidity within the acceptable operating range, humidifiers are used, which are placed before the fuel cell to wet the ingoing gases. While humidification of the gases are vital for good performance, excess water can damage the PEMFC due to water condensation which can block the porous structures of the GDLs and CLs, which limit mass transportation.

The humidity is often expressed in terms of relative humidity (RH), which measures the water vapour pressure, P_{W}, relative to the water saturation pressure, P_{sat}, at the specific temperature,

$$\mathrm{RH} = \frac{P_{\mathrm{W}}}{P_{\mathrm{sat}}}. \tag{3.4}$$

RH is highly depended on temperature and pressure. At higher temperatures, the water saturation pressure increases. Thus when heating gas with a given water pressure, without adding water, the relative RH will decrease, while an increased pressure will decrease the boiling point, and thus increase the RH if no water is added or removed. For example, if a gas at 20 °C and with 100% RH is heated up to 80 °C without adding any more water, the new RH will only be a minuscule 2.4%.

3.1.1.6 Supporting Hardware

Further supporting hardware and software is needed for the fuel cell system to function. Gaskets are used in the MEA to prevent leakages of gases from the porous edges of the CL and GDL, prevent fuel shortcuts and control the compression of the GDLs [84]. Gases needs to be supplied and controlled, and since fuel cells are often operated under elevated pressures to increase activity, pressure systems are often needed. The end plates of the fuel cell/stack provide even pressure, which is important for compression of GDL and to decrease contact resistance [85].

The fuel cell also need some kind of heat management system [86]. In small scale research system, the fuel cell itself and gas pipes often need to be heated to reach the desired operating temperature. In real applications however, the fuel cell will produce much heat by itself, and cooling is needed instead. Cooling can for smaller fuel cells be done through the flow of reactant air. For slightly larger systems, separate air channels purely for cooling can be used if the reactant air cannot remove heat fast enough. For systems over 10 kW, water cooling is usually employed instead [87], since much less volume of water is needed to remove the same amount of heat, and the water can go through smaller channels, thus allowing for smaller and more compact systems to be designed.

3.1.2 Reaction Pathways

In the acidic conditions of the PEMFC, two pathways for the ORR have been identified [88]. Water is formed either via the 2-electron pathway with intermediate peroxide formation

$$\mathrm{O_2 + 2H^+ + 2e^- \rightarrow H_2O_2} \qquad \mathrm{E = 0.67\ V_{RHE}}, \tag{3.5}$$

$$\mathrm{H_2O_2 + 2H^+ + 2e^- \rightarrow 2\,H_2O} \qquad \mathrm{E = 1.77\ V_{RHE}}, \tag{3.6}$$

or via the direct 4-electron pathway

$$\mathrm{O_2 + 4H^+ + 4e^- \rightarrow 2\,H_2O} \qquad \mathrm{E = 1.23\ V_{RHE}}. \tag{3.7}$$

Peroxide formation is favoured at potentials below 0.5 $\mathrm{V_{RHE}}$ leading to low energy conversion efficiency, and can accelerate the degradation of the membrane, thus the 4-electron pathway is favoured [89]. Peroxide can also be formed by hydrogen crossover via the membrane from the anode to the cathode, for why it is necessary to prevent hydrogen cross-over.

Nørskov et al. [35] have suggested two mechanisms for the 4-electron pathway: the first mechanism is called dissociative, where the oxygen dissociates on the surface before being hydrogenated,

$$\mathrm{O_2 + 2^* \rightarrow 2O^*} \tag{3.8}$$

$$\mathrm{O^* + H^+ + e^- \rightarrow OH^*} \tag{3.9}$$

$$\mathrm{OH^* + H^+ + e^- \rightarrow H_2O\ +\ ^*} \tag{3.10}$$

and the other one is called associative, where $\mathrm{O_2}$ react directly with H^+ on the surface,

$$O_2 + {}^* \rightarrow O_2^* \tag{3.11}$$

$$O_2^* + H^+ + e^- \rightarrow HO_2^* \tag{3.12}$$

$$HO_2^* + H^+ + e^- \rightarrow O^* + H_2O \tag{3.13}$$

$$O^* + H^+ + e^- \rightarrow OH^* \tag{3.14}$$

$$OH^* + H^+ + e^- \rightarrow H_2O + {}^*, \tag{3.15}$$

where * denotes an active site on the catalyst surface [35]. While peroxide is not part of the associative mechanism, peroxide can be formed instead of water in Eq. 3.13.

In contrast to the complicated ORR, the HOR is a much simpler reaction, whose elementary steps have been described by Tafel, Heyrovsky and Volmer [90],

Tafel $$H_2 + 2^* \rightarrow 2H^*, \tag{3.16}$$

Heyrovsky $$H_2 + {}^* \rightarrow H^* + H^+ + e^-, \tag{3.17}$$

Volmer $$H^* \rightarrow H^+ + e^-, \tag{3.18}$$

where two of the steps described in Eqs. 3.16, 3.17 and 3.18, either Tafel–Volmer or Heyrovsky–Volmer, take place. Since the ORR involves more electron transfers and intermediate species than the HOR, it has a much slower reaction rate, by several orders of magnitude [91]. Thus, the ORR is the rate limiting step in the fuel cell performance. The large overpotentials caused by the ORR leads to large losses, and most research on the topic of catalysts for fuel cells are focused on the ORR rather than the HOR. Still, some research is being put into the HOR to find alternative catalyst with e.g. better tolerance for CO [92–94].

3.1.3 Figures of Merit

For real life applications, some key operating parameters are used to compare fuel cells with other power generators. For the electrodes, the current density j (current per unit area) is the core parameter. For ease of comparison between fuel cell systems of different dimensions and design, the current is usually normalised, either by geometrical surface area (j_{geo} [A $\text{cm}_{\text{geo}}^{-2}$]), electrochemical surface area (j_{ECSA} [A $\text{cm}_{\text{geo}}^{-2}$]) or per mass of catalyst (j_{mass} [A $\text{g}_{\text{cat/Pt}}^{-1}$]), and the current is given for a specific voltage, normally 0.6 or 0.7 V_{RHE}. Figures of merit such as power per area, specific power (kW kg^{-1}) and power density (kW m^{-3}) are important when comparing between alternative power generators. Other important parameters for successful commercialisation includes cost of production and cost per kW as well as efficiency, lifetime and issues of degradation.

Quantity	**Reactants** (kJ mol^{-1})		**Product** (kJ mol^{-1})	**Difference** (kJ mol^{-1})
	H_2	O_2	H_2O	Δ
G_f°	0	0	-237.14	-237.14
H_f°	0	0	-285.82	-285.82

Table 3.1: Gibbs free energy of formation, G_f°, and enthalpy of formation, H_f°, at standard temperature and pressure for H_2, O_2 and H_2O. Values from [95, 96].

3.1.3.1 Efficiency

The efficiency of a fuel cell is dependent on several variables. Firstly, the theoretical upper limit for the efficiency is given by thermodynamics. Reorganising Eq. 2.5 gives the the maximum theoretical potential that can be achieved by a specific reaction as

$$E = -\frac{\Delta G}{nF}. \tag{3.19}$$

At standard state (20 °C and 1 bar), the change in Gibbs free energy of formation for formation of water (Eq. 3.1) is ΔG_f° = -237.14 kJ mol^{-1}, see Tab. 3.1. Using Eq. 3.19 with $n = 2$ electrons we get

$$E = -\frac{\Delta G_f^\circ}{nF} = 1.23 \text{ V}, \tag{3.20}$$

which is the theoretical maximal voltage that can be achieved for Eq. 3.1 when no current is drawn, also known as open circuit voltage (OCV). When current starts to flow, energy will be lost to e.g. internal resistance, which will be discussed in more detail later.

One can also look at the maximal efficiency for a PEMFC. The efficiency of a chemical reaction is the the ration between the useful energy, ΔG, and the total energy, given by the change in enthalpy ΔH. The change in enthalpy for the formation of water at standard conditions is ΔH_f° = -285.82 kJ mol^{-1}, see Tab. 3.1, which results in a maximum efficiency of

$$\epsilon = \frac{\Delta G_f^\circ}{\Delta H_f^\circ} = \frac{-237.14}{-285.82} = 83\%. \tag{3.21}$$

This can be compared to the maximum efficiency of a combustion engine engine operating at $T_H = 400\,^\circ$C with an exhaust temperature of $T_C = 50\,^\circ$C, which is limited by the Carnot efficiency to

$$\epsilon_{\text{Carnot}} = \frac{T_H - T_C}{T_H} = 52\%. \tag{3.22}$$

In real fuel cells, the voltage will never be 1.23 V_{RHE}, and the efficiency will be less than the maximum 83%. In a realistic system, the efficiency is somewhere around 60% at 0.8 V_{RHE}. This loss of efficiency is cause by overpotentials. Different types of voltage losses such as fuel crossover, activation losses, ohmic losses and mass transport losses will be dominant in the low, medium and high current regions, see Fig. 3.7.

Fuel Crossover Small amounts of H_2 can cross over from the anode to the cathode via the membrane and react directly with O_2 to form water. This leads to a mixed potential, which results in noticeable voltage drops of OCV of around 200 mV from the theoretical value of 1.23 V_{RHE} down to around 1.0 V_{RHE}. Apart from leading to loss of efficiency, when fuel crosses over and react directly with O_2 at the cathode, H_2O_2 can be formed, which degrades the PEM [73, 97].

Activation Losses At low currents, the voltage loss is dominated by activation barriers. Slow kinetics and sluggish reactions needs to be overcome by applying higher overpotentials, which leads to a highly non-linear loss of voltage in the low current region.

Ohmic Losses Once the kinetic barriers have been overcome, the drop in voltage will mainly come from internal resistance in the fuel cell from e.g. ion conduction in the the membrane and contact resistance between CL and GDL. This ohmic resistance regime is characterised by a linear dependence between the voltage and current, also called resistance loss.

Mass Transport Losses At high currents, the mass transport of reactants to the reaction site will not be fast enough to sustain the fast reaction rates, and the current will stagnate, no matter how much overpotential is applied.

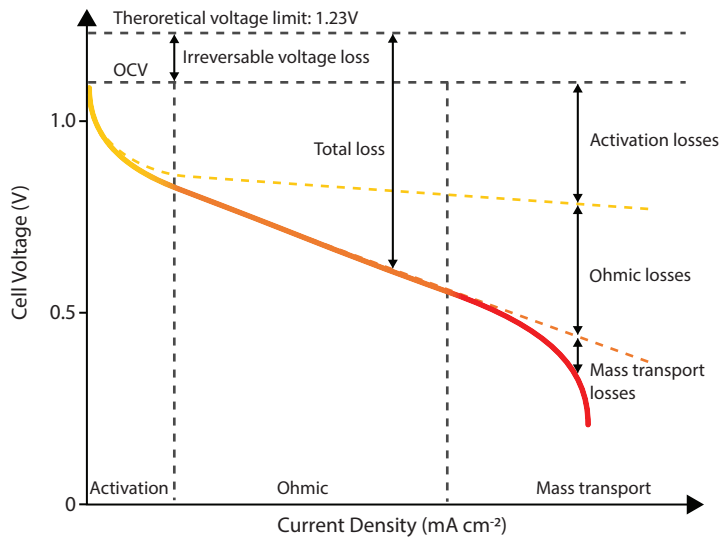

Figure 3.7: Characteristic voltage vs. current curve of a fuel cell, showing the different types of losses associated with low, medium and high current regions.

3.1.3.2 Fuel Cell Degradation

As mention in Chapter 1, one of the key issues of PEMFC is lifetime, related to the harsh conditions of a PEMFC. Some of these harsh conditions promoting degradation in fuel cells include potential cycling, start-up/shutdown cycles, freeze/thawing cycles, humidity cycling and poisoning, each affecting different parts of the fuel cell.

Potential Cycling At normal operation, a PEMFC should be operated below 1.0 V_{RHE}. When the fuel cell is under no or low load, the potential will be close to OCV, at around 0.9–1.0 V_{RHE}. When the load increases, the voltage will decrease to provide a current density to mach the demand, see Fig. 3.7. Under normal operation, the cell voltage will thus continuously cycle between roughly 0.6 and 1.0 V_{RHE}. Looking back at the Pourbaix diagram for Pt (Fig. 2.4b), Pt goes from its metallic state to an oxidised state somewhere between 0.9 and 1.0 V_{RHE}. That means that during during normal fuel cell operation, Pt will repeatedly cycle between being oxidised and being reduced back to its metallic state, which can induce dissolution and loss of catalyst material [98]. Rapid shifts in potential are particularly harmful, as the surface do not have time to relax and redeposit Pt ions. Furthermore, smaller particles are desirable to maximise mass activity. It has been found that the Pt particles with the highest mass activity have a diameter in the range 2 to 5 nm [45, 46]. However, smaller particles also suffer more from dissolution than larger particles [46]. Apart from loss of material due to dissolution, Pt particles have been shown to degrade by growing by crystallite migration and coalescence, and Oswald ripening, and by particle detachment and redeposition, which are illustrated in Fig. 3.8.

Start-up/Shutdown While the fuel cell should be operated at below 1.0 V_{RHE}, the potential can peak up to 1.5 V_{RHE} if the anode is starved of H_2, which can happen during start-up/shutdown conditions if the fuel supply is not properly managed, or during operation if there is local H_2 starvation due to insufficient fuel supply [99]. Such high potentials are especially harmful for the carbon support. While the carbon oxidation reaction (COR) starts already at 0.207 V_{RHE} [100],

$$C + 2H_2O \rightarrow CO_2 + 4H^+ + 4e^- \qquad E = 0.207\ V_{RHE}, \tag{3.23}$$

very high overpotentials are needed for COR to transpire at any considerable rate, due to the sluggish kinetics of the COR. Above 1.0 V_{RHE}, the effects of COR starts to be noticeable, which means the carbon support will start to degrade. There are also indications that Pt is catalysing the COR, thus exacerbating the issue of support degradation in Pt/C catalyst [101].

Loss of support due to carbon corrosion means Pt particles can detach, and possibly attach somewhere without electrical or ion conductivity, essentially leaving the Pt lost and leading to a decrease of ECSA. Collapse of carbon support at weak points will lead to a compaction of the porous structure of the CL, hindering mass transport of reactants to the catalytic sites. Collapse and

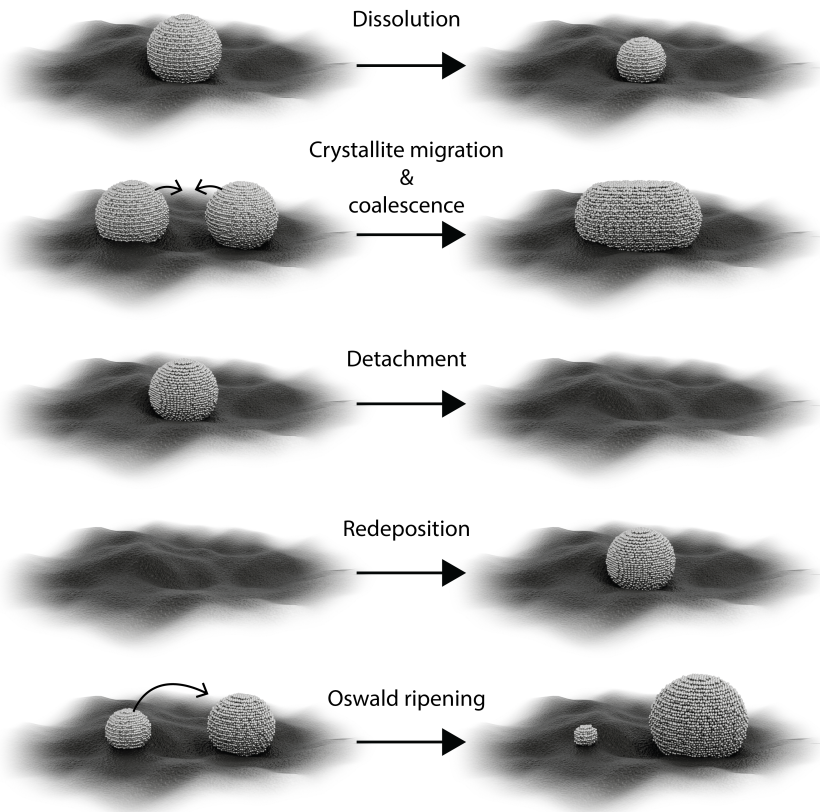

Figure 3.8: Possible degradation mechanisms for catalyst particles.

deformation of the carbon support can also lead to and increase in internal resistance of the cell due to loss of physical contact between Pt, ionomer, support and GDL. All of this leads to massive losses of activity during carbon corroding conditions [102].

Temperature Cycling Some other harsh conditions the fuel cell have to endure is varying temperatures. Fuel cells should be able to cold start from at least $-20\,^{\circ}\mathrm{C}$ [103, 104]. Water is both produced in the MEA during fuel cell operation, and provided externally in the humidified gases. If this water is left in the system after shutdown in subzero temperature, the water will freeze and expand. This causes mechanical damage to the GDLs and CL, and greatly deteriorates the fuel cells performance [103]. Furthermore, during extreme loads, the temperature risk going above $100\,^{\circ}\mathrm{C}$, if the cooling system is not properly dimensioned to handle such events. Such high temperatures can, as discussed in Section 3.1.1.2, degrade the Nafion membrane.

Varying RH The membranes are also sensitive to the humidity levels. Low RH dehydrates the membrane, which reduces its ion conductivity and causes it to shrink. The movement from the membrane swelling and shrinking can cause mechanical damage to the structures e.g. in forms of cracks or tears in the membrane. Damage of the membrane can lead to fuel leakage and crossover, harming the fuel cells performance. Cycling of the RH leads to faster degradation as compared to constant RH conditions [104, 105].

Pin Holes For maximum energy efficiency, the anode and the cathode should be completely separated by the membrane, with only protons being transferred via the membrane. However, pin holes can be generated in in membrane due to physical defects, mechanical stress, fluctuating humidity levels and chemical degradation, which cause hydrogen to crossover from the anodic to cathodic side. Even in the perfect membrane, hydrogen crossover can occur naturally in a small amount. However, pin holes increase the amount of hydrogen crossover, which in turn reduce generated current and further increase degradation.

Chemical Damage & Poisoning The components of the fuel cell also suffers from chemical damage. Fuel crossover can lead to H_2 reacting directly with O_2 at the cathode, creating H_2O_2, which accelerate degradation of the membrane. Impurities in the fuel can also harm performance. For example, CO, which can be present in the fuel e.g. if the H_2 is produced via steam reforming, bind strongly to the surface of Pt, effectively blocking catalytic cites and reducing available ECSA thus poisoning the surface. Furthermore, the highly acidic conditions of the PEMFC, coupled with high potentials and a high humidity environment promotes corrosion of e.g. steel bipolar plates.

Mitigation Strategies While degradation of components is inevitable, it can be minimised. Two main strategies can be used to mitigate degradation issues of PEMFCs and improve their lifetime. Either more durable material

have to be developed, that can withstand the harsh conditions, or the fuel cell conditions needs to be highly controlled, to avoid the most damaging conditions. To implement either strategy, studies need to be done on the effects of different conditions on the different components of the fuel cell, so that degradation mechanisms can be better understood and avoided.

Chapter 4

Methods

In this chapter, I will give a short introduction to some of the techniques the work and results of **Paper I, II** and **III** are based on.

4.1 Electrochemical Measurements

Due to the nature of fuel cells, electrochemical methods and characterisation techniques are tremendously important to fuel cell research.

4.1.1 Set-ups

Often, electrochemical measurements are carried out in an electrochemical cell, where each half reaction of the electrochemical reaction can be studied separately. The simplest version of an electrochemical cell contains two electrodes—one working electrode (WE) on which the half reaction of interest is occurring, and one counter electrode (CE) that acts to balance the charge by acting as an anode or cathode to the reaction on the WE—connected via an electrolyte. A potential is applied between the electrodes, and the resulting current is measured, or vice versa. When currents pass through the CE, its potential will shift, which makes it hard to measure the absolute potential of the WE accurately. To overcome this, a third electrode known as the reference electrode (RE) is added to the system. No current passes through the RE, and thus its potential is kept stable at a known value. The potential of the WE is measured against the RE, while the current is measured between the WE and the CE, see Fig. 5.4. The potential of the RE depends on which reversible reactions it is based on. To simplify comparison between measurements done against different REs, the voltage is often converted to and presented against the potential of hydrogen reduction, also known as the reversible hydrogen electrode (RHE), which is defined as 0 V. During electrochemical measurements, the potential and current are often controlled and measured by a potentiostat, which is a device that can accurately maintain the potential of the WE against the RE.

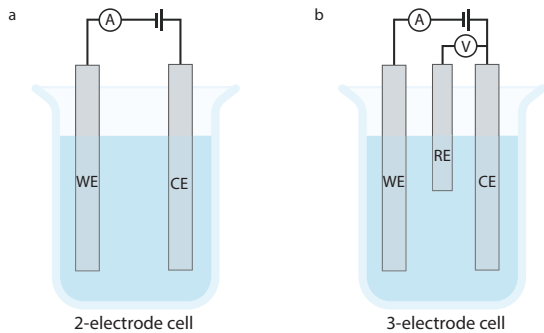

Figure 4.1: Schematic of a) a 2-electrode and b) a 3-electrode cell.

4.1.1.1 Electrochemical Quartz Crystal Microbalance

Quartz crystal microbalance (QCM) is technique where small mass changes can be measured by tracking the variations in the resonance frequency of a quartz crystal. A good set-up can detect changes of less than 1 ng cm^{-2}. In comparison, a mono-layer of Pt weighs around 400 ng cm^{-2} [106]. Quartz is a piezoelectric material, meaning there is a relationship between applied voltage and mechanical deformation. Coating both sides of a quartz crystal disc with an electrode (Fig. 4.2a), and applying an alternating electric field, will induce oscillations (Fig. 4.2b). At a resonance frequency, the amplitude of the oscillations will increase. This resonance frequency will depend on the mass of the crystal. If mass is added, or lost, the frequency will shift.

The Sauerbrey equation relates the change Δf_n of the resonance frequency of the n^{th} overtone to the mass change Δm as

$$\Delta f_n = -n\frac{2f_{0,n}^2}{A\sqrt{\rho_q \mu_q}}\Delta m \tag{4.1}$$

where $f_{0,n}$ is the initial resonant frequency of the n^{th} overtone, A is the area of the electrode, ρ_q is the density of quartz and μ_q is the shear elastic modulus of quartz [107]. The Sauerbrey equation is only valid if certain conditions are satisfied: the films must be rigid and thin, and the change in mass should be small in comparison to the initial mass of the quartz crystal. Preferably, the resultant frequency shift Δf_n should be less than 2% of the initial resonate frequency $f_{0,n}$. If mass changes are larger than this, a more complicated expression than Eq. 4.1 needs to be used, that take into account the difference in density and wave propagation velocity of the quartz and the deposited material. The criteria of the film being rigid can be checked by looking at the change of the dissipation factor

$$\Delta D = \frac{2\Delta\Gamma}{f_{0,1}} \tag{4.2}$$

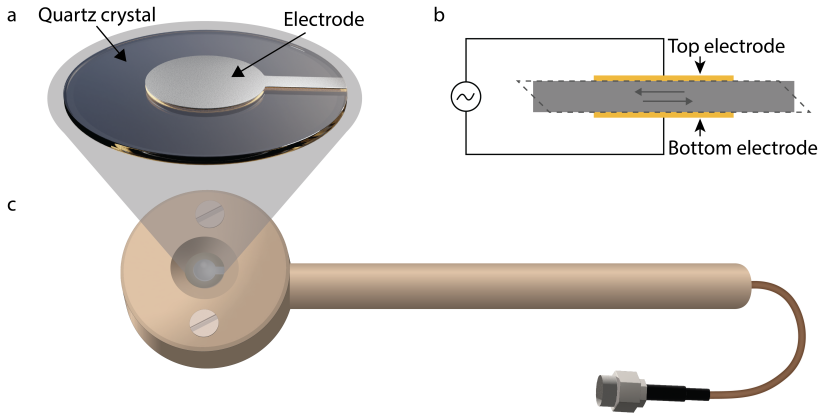

Figure 4.2: a) Typical quartz crystal used for QCM measurements. b) An alternating electrical field is applied over a quartz crystal, which causes it to oscillate. c) Illustration of an EQCM dip-holder. A QCM crystal is coated with one electrode on either side, and the crystal is mounted in the dip-holder such that the electrode of interest is exposed to the outside, and can be used as a working electrode in an electrochemical cell. The dip-holder is made from PEEK, and held together using screws made from nylon. The holder is sealed using o-rings made from FFPM.

where $\Delta\Gamma$ is the change in half bandwidth and $f_{0,1}$ is the initial fundamental frequency. The film is considered rigid if

$$\frac{\Delta D}{\Delta f} \ll \frac{1}{f_{0,1}}. \tag{4.3}$$

QCM can be combined with electrochemical measurements, and is then known as electrochemical QCM (EQCM). In EQCM, one electrode of the QCM is used as working electrode in an electrochemical set-up, allowing for measuring mass changes and performing electrochemical measurements simultaneously. EQCM can be used to measure e.g. mass changes associated with oxide formation during potential cycling, and dissolution rates.

EQCM set-ups comes in many variants, such as flow cells, or dip-holders. Fig. 4.2c illustrates a dip-holder that was used for EQCM measurements in **Paper II**. In it, a quartz crystals coated with a Pt and an Au electrode is mounted in the dip-holder, so that the Pt electrode is exposed to the outside. This allows for using the Pt electrode as a working electrode in an electrochemical cell, while applying an AC field between the Pt and Au electrode to measure the shift in frequency response.

4.1.1.2 Fuel Cell Measurements

While fuel cells intended for commercial applications are often large, and made of stacks, small-scale single cell fuel cells can be used for research purposes,

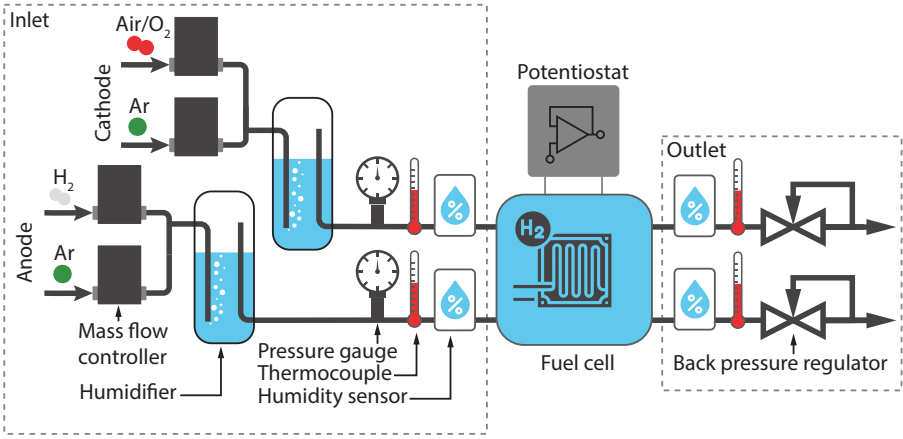

Figure 4.3: Schematic of surrounding control system for single cell fuel cell set-up for research purposes. The humidifiers, tubing and fuel cell are all insulated using glass fibre and heated using heating tape, which is not depicted in the figure.

to study catalyst behaviour under realistic fuel cell conditions. Fig. 4.3 shows the schematic of the the set-up used for measurements in **Paper I** and **Paper III**. The flow rates of the gases and their composition (H_2/Ar for the anode and O_2/Air/Ar for the cathode) are controlled using mass-flow controllers. Before entering the fuel cell, the gases pass through humidifiers to increase their RH. The RH levels of the ingoing and outgoing gases are measured using humidity sensors at the inlet and outlet of the fuel cell. The humidifiers, gas tubes and fuel cell are all heated using heating tapes connected to thermocouples. The temperature of the ingoing and outgoing gases are measured using thermocouples. The pressure of the gases are regulated using back pressure regulators at the outlets, and monitored by pressure gauges at the fuel cell inlet. A potentiostat is used to control and measure the potential and current between the anode and the cathode. During fuel cell measurements, the cathode is acting as the working electrode, and the anode is working both as the counter electrode, and as a reference electrode. This can be done if the anode is under high relative H_2 pressures, as the anode will then act similarly to a reversible hydrogen electrode. This is the case for the cell used in **Paper I** and **Paper II**, since the cell is working under pure H_2 and the cell is relatively small, thus there will not be a substantial difference in H_2 pressure between inlet and outlet of the electrode area. This gives potentials directly in the RHE scale, and removes the need for adding an extra electrode in the set-up which would complicate the set-up greatly. The fuel cell used in this set-up is a 5 cm^2 single cell fuel cell using serpentine graphite flow fields. The MEAs used in the duel cell are assembled according to Fig. 3.6a, and inserted in the fuel cell according to Fig. 3.6b. The compression rate of the GDLs of the MEA are controlled by the use of appropriately thick gaskets made of glass-fibre reinforced Teflon, and the cell is closed using a torque force of 12 N m.

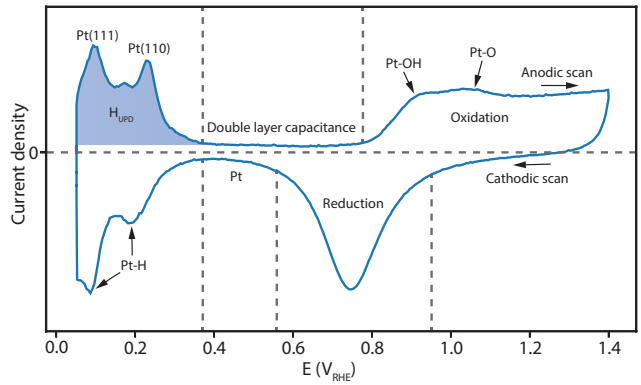

Figure 4.4: Typical CV of polycrystalline Pt in 0.5 M H_2SO_4, measured at a scan rate of 50 mV s^{-1} under inert atmosphere.

4.1.2 Electrochemical Characterisation

Electrochemical reactions have several important characteristic, such as the relationship between voltage and current, that can be probed using various electrochemical methods, some of which will be described here.

4.1.2.1 Cyclic Voltammetry

In cyclic voltammetry (CV), the potential between the RE and the WE is cycled linearly between two potential values, and usually the current is then plotted against the voltage. The resulting plot is commonly also referred to as a CV. CVs can be used to study electrochemical properties of an analyte in the electrolyte solution, or of the electrode surface itself. By convention, positive currents come from positive scan direction, known as anodic currents, and negative currents come from the negative scan direction, known as cathodic currents. In each scanning direction, characteristic peaks will appear from oxidation/reduction of species. These features will depend on the electrode, analyte and electrolyte, and can be used as a fingerprint of sorts to identify materials, if the material in question has any electrochemical reaction taking place in the potential window used.

Of special interest to PEMFC research is the typical CV of Pt in acidic conditions, see Fig. 4.4. Below 0.4 V_{RHE} is the region associated with hydrogen underpotential-deposition and desorption. During cathodic scans, H^+ ions starts to bind to the Pt atoms on the surface, before hydrogen evolution starts at 0 V_{RHE}. During anodic scans, the H^+ adsorbed to the surface will desorb. Different crystal facets of Pt have different desorption potentials, and each peak in the desorption current is thus associate with a specific crystal plane. The CV in Fig. 4.4 show signs of H_{UPD} peaks from the Pt crystal planes Pt{111} and Pt{110} [108, 109].

The flat region between 0.4 and 0.7 V_{RHE} stems from the double layer capacitance. When the potential of the electrode shifts, a surplus or deficit of

charge will accumulate near the surface electrode, even if no other electrochemical reactions are taking place. This will in turn attract ions in the electrolyte, creating an electrical double layer, which acts as a capacitor. The total charge stored in the electric double layer will depend on the applied potential and the electrode surface.

At around 0.9 V_{RHE}, OH binds to the surface, and at 1.0 V_{RHE}, Pt-O starts to form. The surface oxide layer continues to grow at higher potentials, and somewhere after 1.23 V_{RHE}, oxygen evolution will become the dominant process. During cathodic scans, the Pt-O is reduced to metallic Pt at circa 0.8 V_{RHE}.

Electrochemical Surface Area The electrochemical available surface area (ECSA) can be determined from the blue marked region in the CV in Fig. 4.4. Consider the region between 0.0 and 0.4 V_{RHE}. The currents in this region comes from adsorption/desorption of hydrogen to the Pt surface during cathodic/anodic scans, respectively. Every H^+ takes/gives one electron when it is adsorbed/desorbed. Assuming that every Pt atom on the surface has adsorbed one H^+ ion, the total charge associated with hydrogen adsorption Q can be determined by integration the current I versus time t in this region,

$$Q = \int I \; dt = \int I \; dE \frac{dt}{dE} \tag{4.4}$$

where E is the potential and dE/dt is the scan speed. When using Eq. 4.4, the charge associated with the double layer capacitance should be detracted. Dividing Q with the charge of one mono-layer θ, gives the electrochemical surface area

$$A_{\mathrm{ECSA}} = \frac{Q}{\theta}. \tag{4.5}$$

The surface charge θ depends on the metal and the dominant crystal facets. For polycrystalline Pt, the surface charge of one mono-layer of hydrogen is usually set to $\theta_{\mathrm{Pt}} = 210$ µC $\mathrm{cm}_{\mathrm{Pt}}^{-2}$, which is an average of the surface charge of the most common crystal facets [110, 111]. For H_{UPD} on Pt, it is sometimes assumed that integrating from the double layer to the lower peak in the cathodic scan Fig. 4.4 corresponds to a 77% H-coverage [110], which gives the formula for the ECSA as

$$A_{\mathrm{ECSA}} = \frac{\int I \; dE}{0.77 \; \theta \frac{dE}{dt}}. \tag{4.6}$$

Other reactions in the CV can also be used to determine the ECSA in a similar fashion, such as reduction of a metal, CO-adsorption, or the double layer capacitance region.

For fuel cell research, the Pt surface area A is often presented as $\mathrm{m}^2\mathrm{g}_{\mathrm{Pt}}^{-1}$, which is calculated by

$$A_{\mathrm{ECSA/mass}} = \frac{Q}{\theta L A_{\mathrm{geo}}}, \tag{4.7}$$

where L is the Pt loading of the sample ($\mathrm{cm}^2\ \mathrm{mg}_{\mathrm{Pt}}^{-1}$) and A_{geo} is the geometrical surface area of the electrode.

4.1.2.2 Polarisation Curves

The performance of an electrocatalyst can be evaluated using polarisation curves. Polarisation refers to the overpotential, or deviation from the OCV. Polarisation curves are typically plotted as E vs. j or E vs. log j, even if E is the independent variable that is being controlled during the experiment, and shows what overpotentials are needed to reach a certain current density. Polarisation curves can be used to probe reaction kinetics, determine the Tafel slope and exchange current density, and study mass transport limitations. Polarisation curves are performed by linearly sweeping the potential between two end points, in the presence of reactants for the relevant reaction to be studied.

4.1.2.3 Electrochemical Impedance Spectroscopy

Electrochemical impedance spectroscopy (EIS) is a method where the impedance Z is measured by applying an alternating potential E to a system and measuring the current response I, where

$$Z = \frac{E}{I}. \tag{4.8}$$

The impedance Z is often expressed as an imaginary number, where $\mathfrak{Re}\ Z$ corresponds to the normal resistance, i.e. the direct response of the current to the applied voltage, and $\mathfrak{Im}\ Z$ is a phase shifted response of the current, due to capacitive and inductive properties. In EIS, the frequency f of the ac-signal is scanned from high to low frequency, or vice versa, and the resulting impedance $Z(f)$ is plotted either on the imaginary plane in a Nyquist plot, or $\mathfrak{Re}\ Z$ and $\mathfrak{Im}\ Z$ is plotted separately in a Bode plot.

4.1.3 Accelerated Stress Tests

Due to the impracticality of testing fuel cell system for the target lifetimes of up to 30 000 h, accelerated stress tests (ASTs) are used. The aim of using ASTs is to simulate the degradation processes of the materials during real operational conditions, so that the real degradation processes can be studied and understood, but with testing times on the order of days and week, rather than years. There are many different types of ASTs for PEMFCs, aimed at simulating different operation conditions and to separate different types degradation effects, see Fig. 4.5. The ASTs can be divided into static methods, such as potential holding, or dynamic techniques such as different types of potential, humidity or temperature cycling. Typically it is transients between

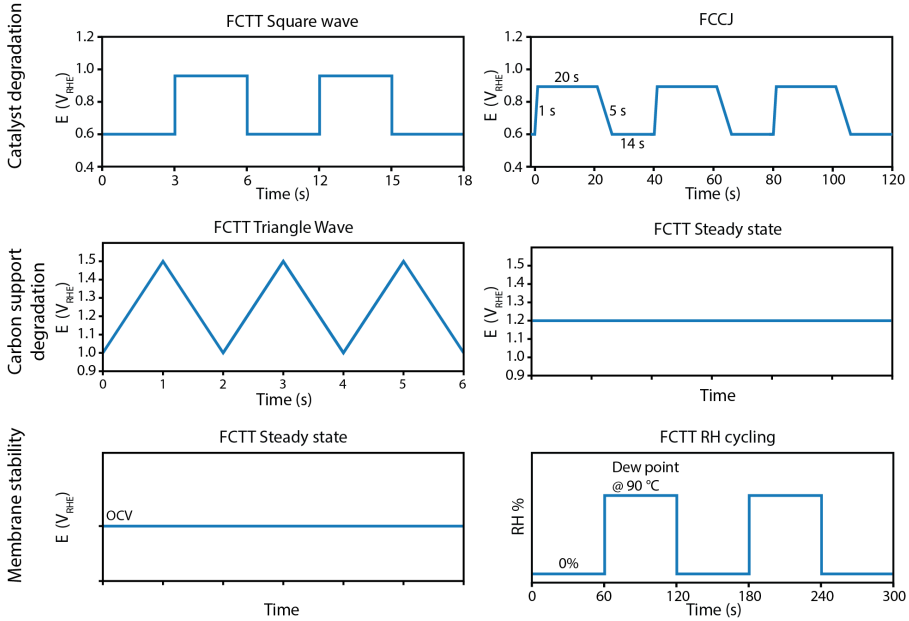

Figure 4.5: Some examples of AST protocols for fuel cell degradation, focused on studying the degradation of either the catalyst, the carbon support or the membrane. Protocols taken from [112, 114, 115].

conditions that are the most detrimental for a fuel cell, rather than static operation conditions, and thus many ASTs are focusing on varying e.g. the potential, load or RH to accelerate the degradation processes. For the potential variations, the faster the potential shift are, the more damage is done to the system. As an example, a study done by Stariha et al. [112] showed that square wave cycling lead to a five time increase in the degradation rate compared to triangular wave cycling in the same potential ranges, due to the faster shifts in potential during square wave cycling.

Voltage cycling in the range 0.6–1.0 V_{RHE} is often performed to simulate normal operation of a fuel cell, while potential cycling between 1.0 and 1.5 V_{RHE} is done to simulate potential spikes that can occur during start-up/shutdown events [21, 112]. Wet/dry cycling of the RH can also be used, sometimes in combination with varying potentials or loads, to study e.g. stability of the membrane [104].

Other types of ASTs aim to simulate representative drive cycles in e.g. a city, where a vehicle would typically need to accelerate and decelerate often, and idle at red-lights and crossings [113].

4.2 Physical Characterisation

Physical characterisation methods are used to gain information about the morphology and chemical composition of a sample, and are important complements to the electrochemical characterisation techniques discussed in Section 4.1.

4.2.1 Electron Microscopy

Scanning electron microscopy (SEM) is a characterisation method where a focused beam of electrons is used to image the surface of a sample. Fig. 4.6a show a schematic of a SEM. A high energy electron beam (around 0.2 to 40 keV) is focused using magnetic lenses and scanned in a raster pattern over a sample. The electrons interact with the atoms in the sample, producing different types of signals such as secondary electrons (SE), back-scattered electrons (BSE) and characteristic x-rays. These signals can give information about the surface topography and chemical composition of the sample. Due to the difference in energies of the SE, BSE and x-rays, they have different mean free paths, and thus the signals will come from different depths in the interaction volume of the sample, see Fig. 4.6b. SE comes from electrons in the outer orbitals of the atoms being knocked out. SE has the lowest energy of the signals, and thus only measures a few nm down in the sample. The signal strength of SE will depend, among other things, on the angle of incidence of the sample compared to the electron beam, and will thus show the topography of the sample. BSE comes from electrons in the electron beam being elastically backscattered from the atoms. Heavier elements backscatter electrons more strongly than lighter elements, thus BSE gives good contrast between areas with different elements. BSE have more energy than SE, hence BSE signals originate from a larger interaction volume than SE.

SEM can be used to study samples from the macro-scale down to the micro- and nanoscale. Under the right conditions, a SEM can reach resolutions of less than 1 nm. Due to the attenuation of electron beams under gas atmospheres, conventional SEM requires imaging to be performed under high vacuum. Furthermore, the sample being imaged should be electrically conductive to prevent charge accumulation and image distortions.

Transmission electron microscopy (TEM) works on similar principles as SEM, but instead of measuring secondary and backscattered electrons, the image is formed by detecting transmitted electrons, see Fig. 4.6a. Due to the de Broglie wavelength of electrons, they will interact with the specimen and form an image plane, much like a normal light microscope works. However, since the wavelength of electrons is on the order of Å, TEM can give a image resolution where single columns of atoms can be detected. Since the electron beam has to be transmitted, the samples have to be thin, preferably $<$100 nm.

Like the SEM, a TEM can be operated in different modes. Normal TEM can be used to either image the sample directly, or to look at the diffraction pattern, which can give you information about either the sample morphology or crystal structure.

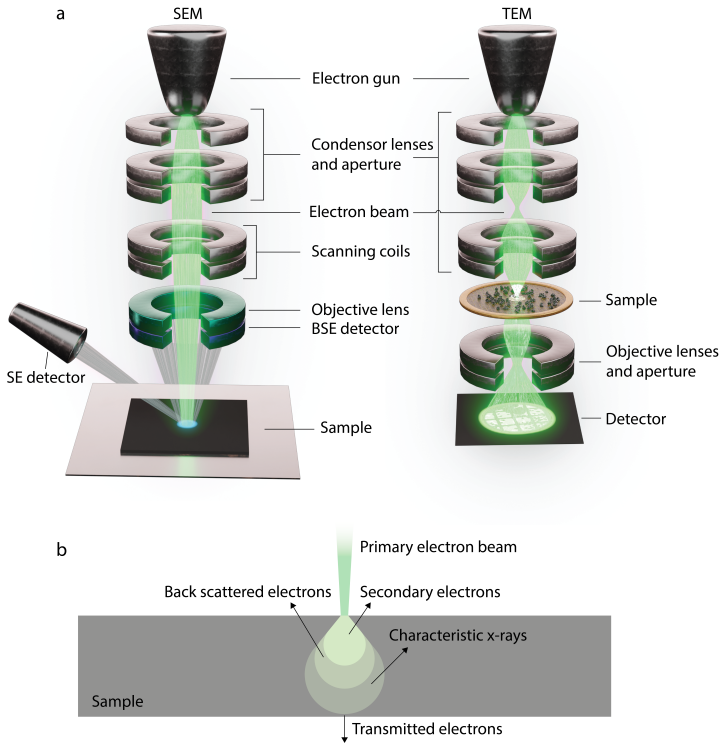

Figure 4.6: a) Schematics over SEM (left) and TEM (right). In both SEM and TEM, a high energy electron beam is focused on a sample using magnetic lenses. In SEM, the beam is scanned in a raster pattern over the surface, and either scattered electrons or characteristic x-rays is detected. In TEM, the electron beam is transmitted through the sample, and the image of the sample is projected on a fluorescent screen or a digital detector. b) Interaction volume of electrons in a sample.

4.2.1.1 Identical Location Micrography

In identical location (IL) SEM and TEM, the same area of the sample is imaged repeatedly. This has the strength of being able to follow changes of the sample on the nanoscopic level, allowing for studying the degradation of individual particles. IL-SEM and IL-TEM can help separate effects which with normal SEM and TEM would not be distinguishable. For example, with IL-SEM and IL-TEM, different types of particle degradation, such as detachment, migration, redeposition, corrosion and dissolution (Fig. 3.8) can clearly be distinguished, which would not be possible without having an initial reference image to compare to. By taking several intermediate IL images during a process, the growth rate of individual particles can be calculated, and the influence of e.g. initial defects can be studied. In **Paper I** and **Paper III**, IL-SEM and IL-TEM was implemented into a real single-cell fuel cell system.

For IL-SEM, an MEA is constructed according to Fig. 3.6 and pressed together in the fuel cell. The MEA is then removed from the fuel cell, and the GDL of the cathodic layer is gently removed exposing the cathodic CCL. The MEA without the cathodic GDL is mounted on an in-house built stage, and inserted into a SEM for imaging of the CCL surface. After SEM imaging, the GDL is placed back on the MEA, and the full MEA is placed back into the fuel cell for electrochemical evaluation. The process of imaging the CCL is then repeated, to follow the surface morphology changes over time. The stage used for SEM imaging ensures the same position of the MEA every time, and by using a coordinate system, the same location can then repeatedly be found and imaged without the need for physical marking of the sample surface.

IL-TEM is performed by introducing a TEM grid with Pt/C deposited on it between the GDL and the CCL of an MEA, constructed similarly as for the IL-SEM imaging. After each AST session, the MEA is removed from the fuel cell, and the cathodic GDL removed to expose the TEM grid, which is gently lifted out for imaging. After TEM imaging, the grid is placed back on the same location of the CCL, the GDL is placed back on the MEA and the full MEA is placed in the fuel cell for electrochemical testing. The TEM grids have a marked grid system, which helps with locating the same area of the sample.

4.3 Sample Preparation

To simplify the systems that are to be studied model electrodes can be used. In particular, in the works included here, thin film electrodes are used. By studying the behaviour of thin films with a well defined surface area, confounding effects such as mass transport limitations, size and shape dependency, and catalyst-support interactions can be separated, and the intrinsic activity and behaviour of the material itself can be studied.

4.3.1 Thin Film Fabrication

Electron-beam (E-beam) evaporation is a type of physical vapour deposition used to deposit thin films of materials. A beam of high-energy electrons is

directed from a filament to an ingot of the target material of choice using magnetic fields. When the beam hits the target, it will heat up rapidly until it starts to melt or sublime, leading to vapours being ejected from the surface. These vapours are used to coat a substrate. The coating thickness is measured using QCM, and E-beam evaporation can be used to create thin films with a thickness of a few Å up to several µm. This method was used in **Paper II** to fabricate 200 nm thick Pt thin films on quartz crystals, for use in EQCM measurements.

4.3.2 Micrography Preparation

Cross sectional samples of CCMs (**Paper I**) and QCM crystals (**Paper II**) were produced using focused ion beam, in which a high energy beam of ions is used to mill through the surface of a sample. In **Paper III**, samples for TEM imaging was prepared by scraping of a powder of Pt/C from the cathodic side of a commercial 3-layer CCM. The powder was dispersed in Milli-Q water, and the solution was drop-casted on TEM grids, which were left to air dry.

Chapter 5

Results

In this chapter, I present some of the results on which **Paper I, II** and **III** are based.

5.1 Mass Response & Dissolution of Pt Thin Films

While studying the catalyst in real fuel cells is immensely helpful to elucidate the real degradation effects, the complexity of the sample and the testing environment means the individual contributions to performance loss and deactivation of e.g. catalyst activity, gas transport through catalyst support and ion conduction through ionomer are hard to separate. To isolate each effect on its own, and understand how it affects the overall performance, simplified model systems are preferred.

Paper II presents EQCM measurements performed on Pt thin films to understand its dissolution rate and mass response behaviour in different electrolytes when scanning to different upper potential limits (UPLs). The behaviour of Pt was studied in H_2SO_4, since it is the electrolyte that most closely resembles the acidic side groups of Nafion used in PEMFC, and in KOH, to investigate how the results of Pt in alkaline conditions compare to the behaviour in acidic conditions, motivated by the current scientific endeavours to develop alkaline alternatives to PEM technologies.

Fig. 5.1a and b show characteristic CVs and corresponding mass responses of a polycrystalline Pt thin film in 0.5 M H_2SO_4, measured using EQCM. The mass response of the Pt thin film can be divided into three different potential regions, corresponding to the regions of different electrochemical processes in the CV. In the hydrogen adsorption/desorption region, below 0.4 V_{RHE}, the surface mass decreases during cathodic scans, when hydrogen adsorbs, and increases during anodic scans when hydrogen desorbs, which might seem counter intuitive. This has to do with the fact that the QCM does not only measure the mass of the surface, but also the mass in the near vicinity of the surface. When hydrogen is adsorbed to the surface, water molecules are

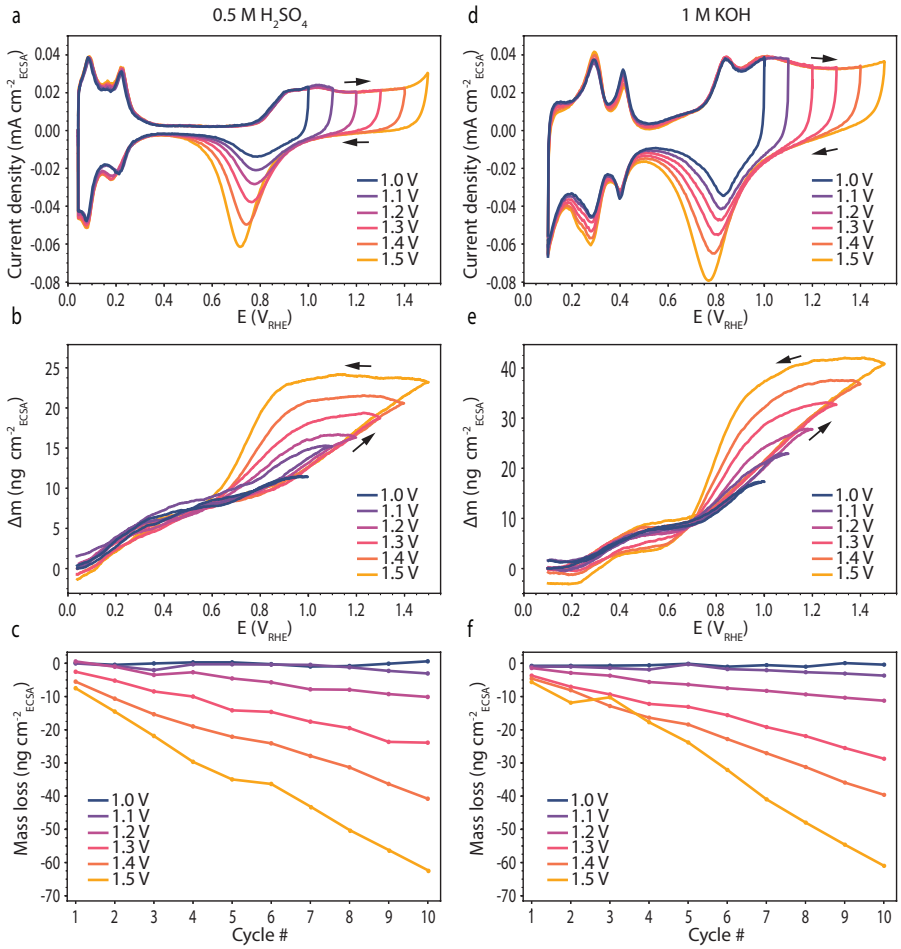

Figure 5.1: CVs, corresponding mass responses and mass loss per cycle of Pt thin films cycled to different upper potential limits in 0.5 M H_2SO_4 (a, b and c) or 1 M KOH (d, e and f) at 50 mV s^{-1} and under inert atmosphere.

displaced, and when hydrogen desorbs, water molecules take their place, thus giving a decrease and an increase of the measured mass, respectively. This decrease during hydrogen adsorption leads to a point of minimum mass, at which all the surface have been fully covered with hydrogen, which for H_2SO_4 occurs at around 0.05 V [116].

After the hydrogen adsorption/desorption region, the mass increases slightly when scanning in the double layer region, due to ions in the electrolyte being attracted to the vicinity of the electrode surface. After 0.8 V_{RHE} during anodic scans, the Pt surface starts to increase in mass more rapidly due to oxidation of the surface, which proceeds in steps. First, OH ions are being bound to the surface, and at around 1.0 V_{RHE} PtO begins to form. The mass gained during oxidation, >0.8 V, scales roughly linearly with the UPL. When the scan direction is reversed during cathodic scans, the mass is roughly stable until a potential of 0.8 V_{RHE} is reached. Below 0.8 V_{RHE} the mass decreases rapidly, as the PtO is being reduced back to metallic Pt. At circa 0.6 V_{RHE}, all the oxide mass has been reduced.

Fig. 5.1c, shows the dissolution rate of the Pt thin film, during potential cycling to different UPLs. At an UPL of 1.1 V_{RHE} or below, little to no mass is lost per cycle. When cycling to higher potentials, the surface starts to lose mass, and the amount of mass lost per cycle scales with the UPL. Pt is dissolved during cathodic scans, when PtO is reduced back to metallic Pt. During this reduction, Pt has to settle back into its metallic state, and oxide have to be released from within the surface layer. At slower scan rates, or when the PtO layer is thin, the Pt is more likely to settle back on the surface. At higher scan rates, or when the PtO layer is thicker, Pt ions are less likely to redeposit on the surface, and is more likely to be washed away in the electrolyte.

Thus, during normal fuel cell conditions, when the potential is cycled between 0.6 and 1.0 V_{RHE}, the results in Fig. 5.1c indicate that very little Pt should be lost through dissolution. It could also indicate that any Pt that is dissolved is likely to redeposit on nearby particles rather than being washed away, which would result in particle growth through Oswald ripening.

Fig. 5.1d and e show characteristic CVs and corresponding mass responses of a Pt thin film in in1 M KOH. The CVs are distinctly different than when measured in H_2SO_4, showing clearly how CVs are highly specific for the combination of electrolyte and electrode material. Even so, the currents in the different regions have similar characteristics and origins as when measured in H_2SO_4.

At lower potentials, <0.5 V_{RHE}, the currents comes from underpotential deposition/desorption of hydrogen. Notably, these peaks are shifted towards higher potentials as when compared to the CV in Fig. 5.1a. Above 0.8 V_{RHE} in the anodic scan, the current from oxidation is larger in Fig. 5.1d than in Fig. 5.1a, and during cathodic scans, the reduction of the surface oxide starts at a slightly higher potential. Furthermore, the double layer capacitance in Fig. 5.1d is less well defined than in Fig. 5.1a, due to a higher onset potential for the hydrogen deposition.

These differences are reflected in the behaviour of the mass response, see Fig. 5.1e. Starting at the hydrogen adsorption/desorption, the mass response

in Fig. 5.1e have a noticeable plateau below 0.2 V_{RHE}, corresponding to the peak during hydrogen adsorption in Fig. 5.1d. This is analogous to the point of minimum mass previously identified in H_2SO_4 at around 0.05 V_{RHE} and correlated to the point at which a full layer of hydrogen has been adsorbed to the surface [116], and indicates that a full hydrogen layer is formed at a higher potential in KOH. During oxidation, more mass is gained in KOH than in H_2SO_4, corresponding to the higher current density in the CVs from the KOH. Also, during reduction, the mass reduction in Fig. 5.1e starts more or less immediately, albeit at a slower pace in the beginning, in contrast to the plateau in Fig. 5.1b, which is in agreement with the earlier onset in reduction seen in Fig. 5.1d compared to Fig. 5.1a.

Based on the larger amount of mass gained during oxidation in alkaline electrolyte, one might be lead to think that Pt would be more prone to dissolution in alkaline environments, since when more PtO is formed and reduced, the likelihood of Pt redepositing should be decreased. However, that is not what was observed. Despite the differences in behaviour of the CVs and mass response between Pt measured in H_2SO_4 and KOH, the dissolution rate per cycle and per UPL is comparable in either electrolyte, see Fig. 5.1. As in H_2SO_4, no dissolution is seen when cycling to 1.0 V_{RHE}. At 1.1 V_{RHE} and above, the dissolution rate scales with UPL, and the values are similar for both H_2SO_4 and KOH. This indicates that the stability of Pt is similar in either electrolyte, and that the potential ranges at which the cell is operated are more important to lifetime and degradation rather than the pH.

5.2 Accelerated Stress Tests

To study degradation of Pt/C catalyst under real fuel cell conditions, samples for IL-SEM and IL-TEM are prepared according to Section 4.2.1.1 and Section 4.3.2. After initial imaging, these samples are inserted in a 5 cm^2 fuel cell with surrounding control system as described in Section 4.1.1.2. Before stress testing and electrochemical characterisation, the MEA is subjected to a conditioning procedure. After, the sample is subjected to an AST cycling protocol, including recovery procedures, electrochemical characterisation AST sessions and IL-SEM/TEM imaging. An overview of the procedure is shown in Fig. 5.2a, and a full description of the experimental method can be found in **Paper I** and **III**.

The degradation have been studied for two different types of ASTs, see Fig. 5.2b. To study catalyst degradation under normal operation conditions, a square wave potential profile is used where the potential is held at 0.6 V_{RHE} for 8 s, and then at 1.0 V_{RHE} for 8 s, for an over cycle length of 16 s. To study the effects of start-up/shutdown events, a triangular wave AST is used where the potential is scanned between 1.0 V_{RHE} and 1.5 V_{RHE} at a scan rate of 500 mV s^{-1}. Both ASTs are performed at 80 °C, with fully humidified H_2/Ar at anode/cathode and under atmospheric pressure.

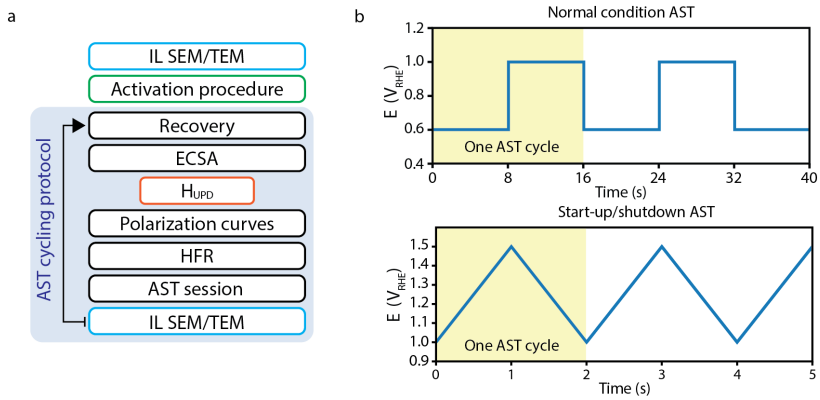

Figure 5.2: a) Test protocol for IL-SEM/TEM studies. b) AST profiles for simulating normal operation conditions (upper) and start-up/shutdown conditions (lower).

5.2.1 Method Verification

Degradation studies where the the MEA has been disassembled and imaged under vacuum mid run have not previously been presented. To ensure the imaging process itself did not cause extra harm to the sample, and that only the AST cycling was causing the degradation of the samples, two test runs were made using the normal condition AST: one with intermediate IL-SEM imaging, and one reference run without any disassembling or intermediate SEM imaging. Both experiments were performed on samples from the same batch, giving similar starting points of the polarisation curves, HFR and CVs. Electrochemical characterisation from the two runs show no discernible difference in degradation, neither in polarisation curves, HFR, CVs or ECSA, see Fig. 5.3. From this, we conclude that disassembling the fuel cell, removing the cathodic GDL, and imaging the MEA under vacuum does not lead to extra degradation of the surface, and that behaviour we see of the CL via IL-SEM is indicative of the true degradation processes.

5.2.2 Degradation of Performance

Fig. 5.4a and b shows polarisation curves and HFR from normal conditions AST and start-up/shutdown AST, respectively. Both experiments were performed on MEAs from the same batch, giving similar polarisation curves and HFR at BOL. During the normal operation AST, the polarisation decreases slightly, from 251 mA cm^{-2} at BOL to 183 mA cm^{-2} at EOL, at 0.7 V_{RHE}. In contrast, during the start-up/shutdown AST, the polarisation curves decreases much more rapidly. After 500 start-up/shutdown cycles, the polarisation has decreased by about 105 mA cm^{-2} at 0.7 V_{RHE}. Further cycling kills the sample completely, with the polarisation decreasing from 244 mA cm^{-2} at BOL to 28 mA cm^{-2} at EOL, at 0.7 V_{RHE}.

The loss of activity also correlates to an increase of resistance (Fig. 5.4a and

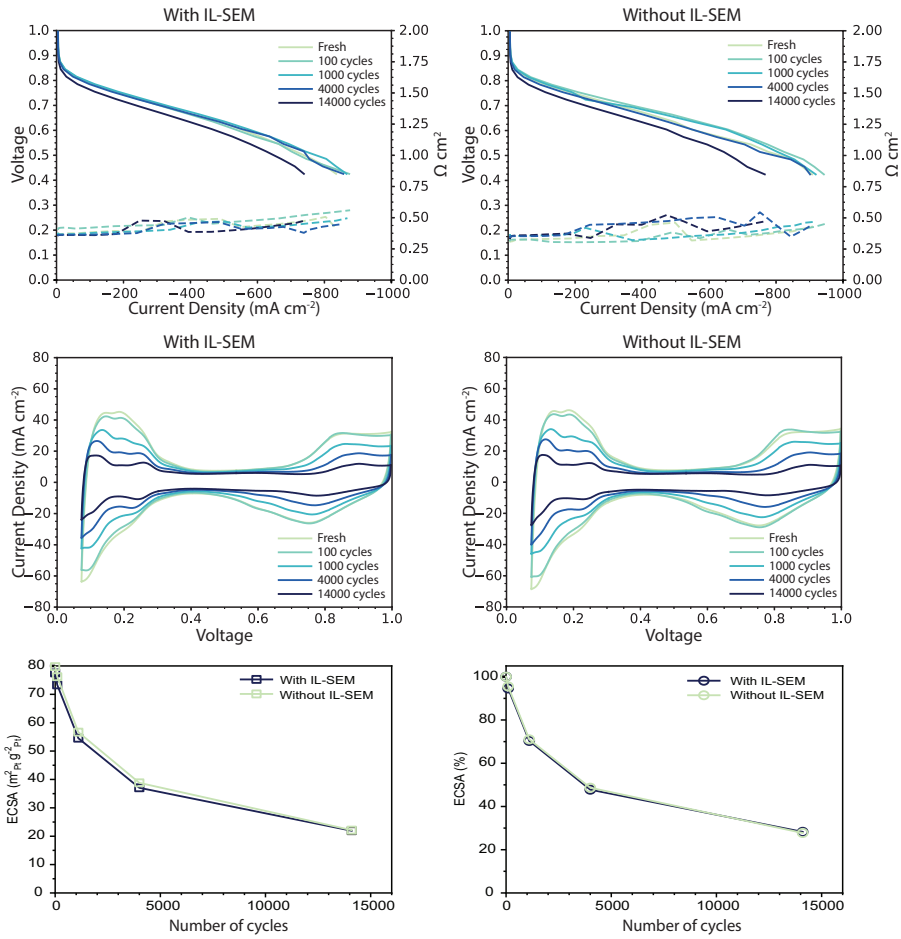

Figure 5.3: Polarisation curves, high frequency resistance, CVs and ECSA for an experimental run with intermediate IL-SEM, and a reference run without intermediate IL-SEM.

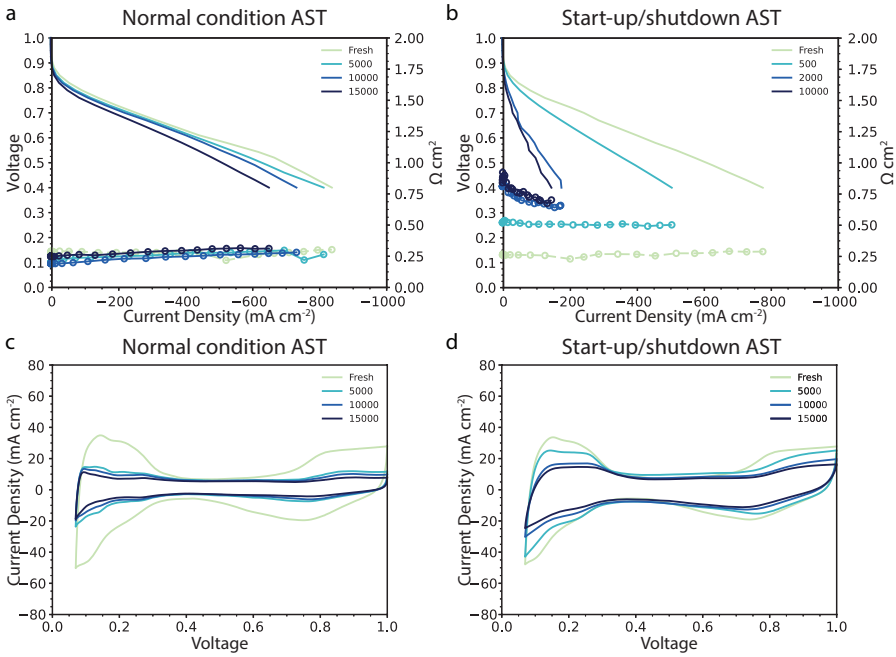

Figure 5.4: Polarisation curves, HFR and CVs from a) and c) normal condition AST and b) and d) start-up/shutdown AST.

b). The resistance is fairly stable during normal condition AST, at around 0.25 Ω cm^2. During start-up/shutdown cycling, the resistance increases noticeably. Already after 500 cycles, the resistance has more than double to over 0.50 Ω cm^2, and at EOL the resistance have increased by 3–4 times from its initial value.

The CVs show typical electrochemical behaviour of Pt/C at BOL for both ASTs (Fig. 5.4c and d), with visible peaks for hydrogen adsorption/desorption between 0.07 and 0.4 v_{RHE}, the double layer capacitance between 0.4 and 0.7 V_{RHE}, and Pt oxidation/reduction at around 0.8–1.0 V_{RHE}. The CVs resembles that CVs measured when cycling up to 1.0 V_{RHE} in 0.5 M H_2SO_4 (Fig. 5.1, although the individual peaks at H_{UPD} for different crystal planes are more pronounced for the well structured Pt thin film, than it is for the Pt nanoparticles on carbon support. After AST cycling, the hydrogen adsorption/desorption peaks, and the Pt oxidation/reduction peaks are decreasing in size. During normal condition AST, the double layer capacitance is left constant, while during start-up/shutdown AST, the double layer capacitance first increases, and thereafter is reduced.

The ECSA was calculated from the CVs from the hydrogen desorption peaks using Eq. 4.7, with a cathodic Pt load of 0.4 mg cm^{-2} and assuming a full surface coverage. Both ASTs result in major decrease of the ECSA. Interestingly, the ECSA decreases less during start-up/shutdown AST than during normal condition AST, despite the opposite trend in activity. During

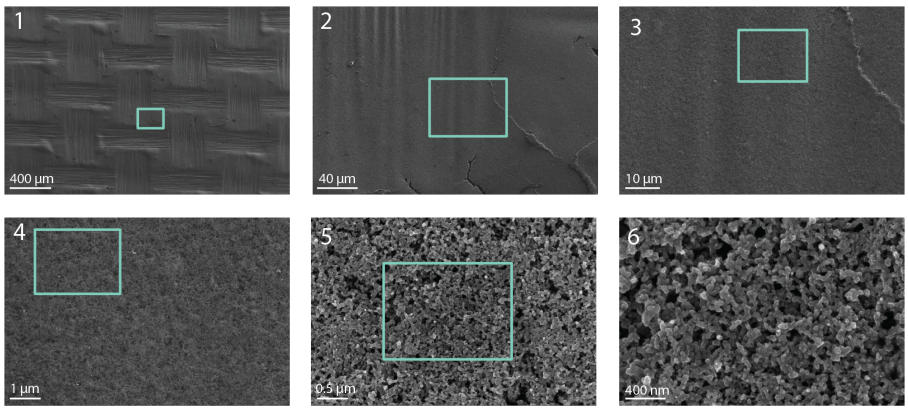

Figure 5.5: Series of SEM images from 100 X magnification down to 100 000 X magnification from BOL, illustrating how the area of the sample was located by gradually zooming in. Blue rectangles show where the next image in the series were taken.

normal condition AST, the ECSA decreases by circa 85% from 62 to 9 $m^2 g_{Pt}^{-1}$, while during start-up/shutdown AST, the ECSA decreases only 68%, from from 62 to 20 $m^2 g_{Pt}^{-1}$.

5.2.3 Particle Growth & Support Degradation

The electrochemical results from Section 5.2.2 can be better understood when looking at the IL-SEM and IL-TEM imaging. The IL-SEM imaging shows the degradation processes on a macro-scale, while the IL-TEM imaging shows what occurs on a nanoscopic scale. Together, these images give a more full view of the degradation processes than either method would on their own.

Fig. 5.5 shows a series of SEM images at different magnifications, showing how the same area was located by gradually zooming in on the sample. Blue rectangles show area of respective image where the next image in the series where taken from. Fig. 5.6 shows IL-SEM images from BOL and after 1000, 4000 and 10 000 normal condition AST cycles at 100 X, 15 000 X and 250 000 X magnification.

On the IL-SEM images, the CCL seems stable during normal condition AST, with no visible changes to the carbon support (Fig. 5.6). Changes are seen first when looking closely at high magnification images (Fig. 5.7). At BOL, the SEM images show the spherical carbon support particles (grey/black spheres), with very few visible Pt particles (white dots) scattered throughout the support. More Pt particles are present, but they are too small to be seen with SEM at BOL. With TEM imaging however, the Pt is easily visible at BOL, as black particles in the size of around 4 nm (Fig 5.8). After AST cycling, the Pt particles are seen move towards each other. These Pt particles then merge, slowly forming larger particles, which are often elongated in shape. Eventually,

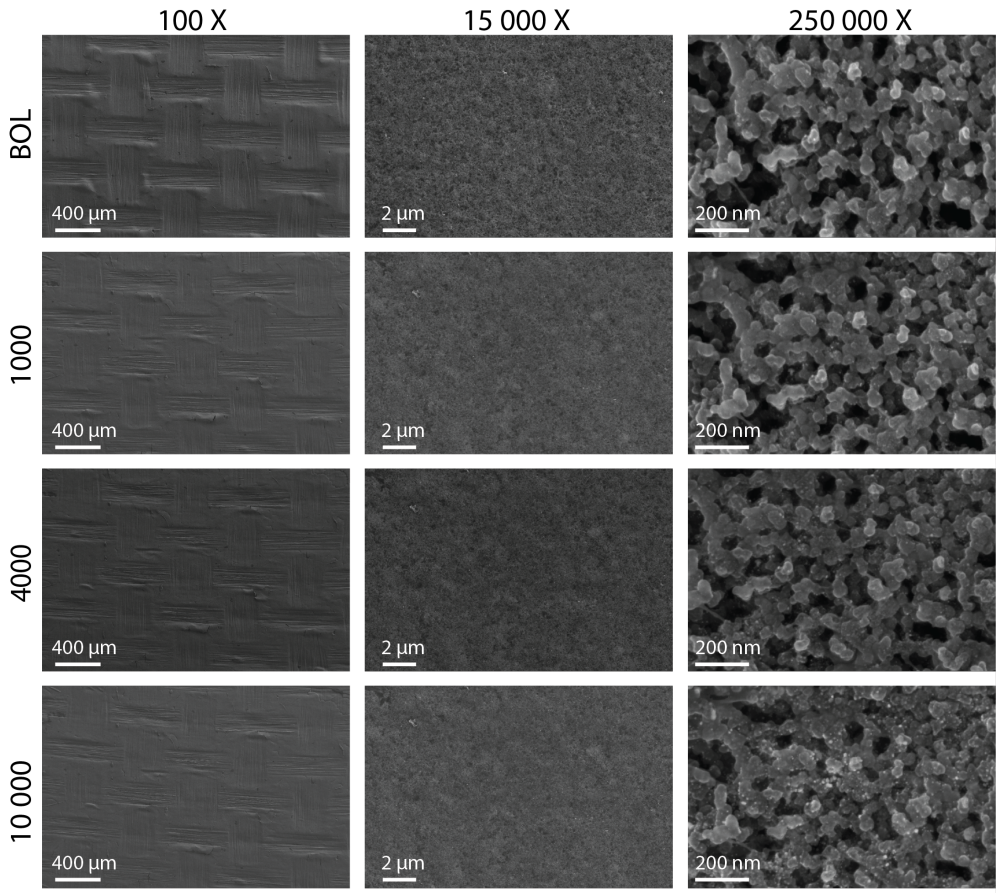

Figure 5.6: IL-SEM images from BOL, and after 1000, 4000 and 10000 total cycles at 100 X, 15 000 X and 250 000 X magnification.

the TEM images show that the initially smaller particles form clusters are large enough to be seen by SEM, which is the reason why Pt particles are seemingly popping up from nowhere in the SEM images after AST cycling. Larger Pt particles are also seen to grow, in tandem with smaller neighbour particles shrinking, indicating Oswald ripening. Furthermore, some Pt particles are disappearing, without neighbour particles to have merged with, indicating that these particles might have detached. Overall, the most prevalent mode of growth seem to be migration and coalescence, with some Oswald ripening. This results in an increase of average particle size, from 3.4 nm at BOL to 4.4 nm at EOL, as measured from the TEM images. While growth of particles does mean less available surface area per gram of Pt, this growth is not enough on its own to fully explain the extensive loss of ECSA seen during normal condition AST. Assuming no mass is lost, the size increase in Fig. 5.10a) only correlates to a decrease of ECSA of less than 25%. Thus other processes must take place as well to explain the 85% loss of ECSA. Part of the reason for this discrepancy could be the IL-SEM and IL-TEM imaging only shows the degradation on the CL nearest to the GDL, and that the degradation throughout the CL is not necessarily homogeneous. For example, Pt particle tend to accumulate closer to the membrane, and Pt ions are known to diffuse into the membrane, to form Pt particles in the membrane when reacting with crossover hydrogen [117]. Particles inside the membrane are not in electrical contact with the rest of the CL, and thus the mass of those particles is essentially lost, and will not contribute to available ECSA.

As for the carbon support, only minor changes are seen throughout the normal condition AST. Overall, the support is stable, and show little sign of loss of volume or other forms of deformation both in IL-SEM and IL-TEM imaging. This is expected since the relatively low potential range is not enough to drive COR. Only close inspection of the IL-SEM and IL-TEM images do show minor changes to the carbon support, with carbon particles shifting or sometimes detaching, possibly due to mechanical damage during handling.

IL-TEM images from the start-up/shutdown AST show different modes of degradation compared to normal condition AST. While the initial state at BOL are similar, difference in behaviour is found already after a few hundred cycles, see Fig. 5.9. Before 500 cycles, weak points in the carbon support collapses, resulting in large parts of the sample being lost. The carbon on the remaining sample is seen to shrink in size, indicating loss of volume and mass due to carbon corrosion at the high potential cycling. When the carbon support shrinks, so does the distance between Pt particles, which promotes coalescence and particle growth. At EOL, large Pt particles, above 15 nm in diameter, are seen all throughout the sample. Many of these particles cannot be explained by the initial Pt particles in that area merging, indicating that Pt particles at other locations have detached due to loss of support, and reattached on whatever support remains.

Overall, even though the ECSA decreases less, the Pt particles grow more during the start-up/shutdown AST compared to normal conditions AST, from 3.2 nm at BOL to 5.4 nm at EOL. Still, the particle growth itself is not enough to explain the loss of ECSA, showing again that other effects not discernible

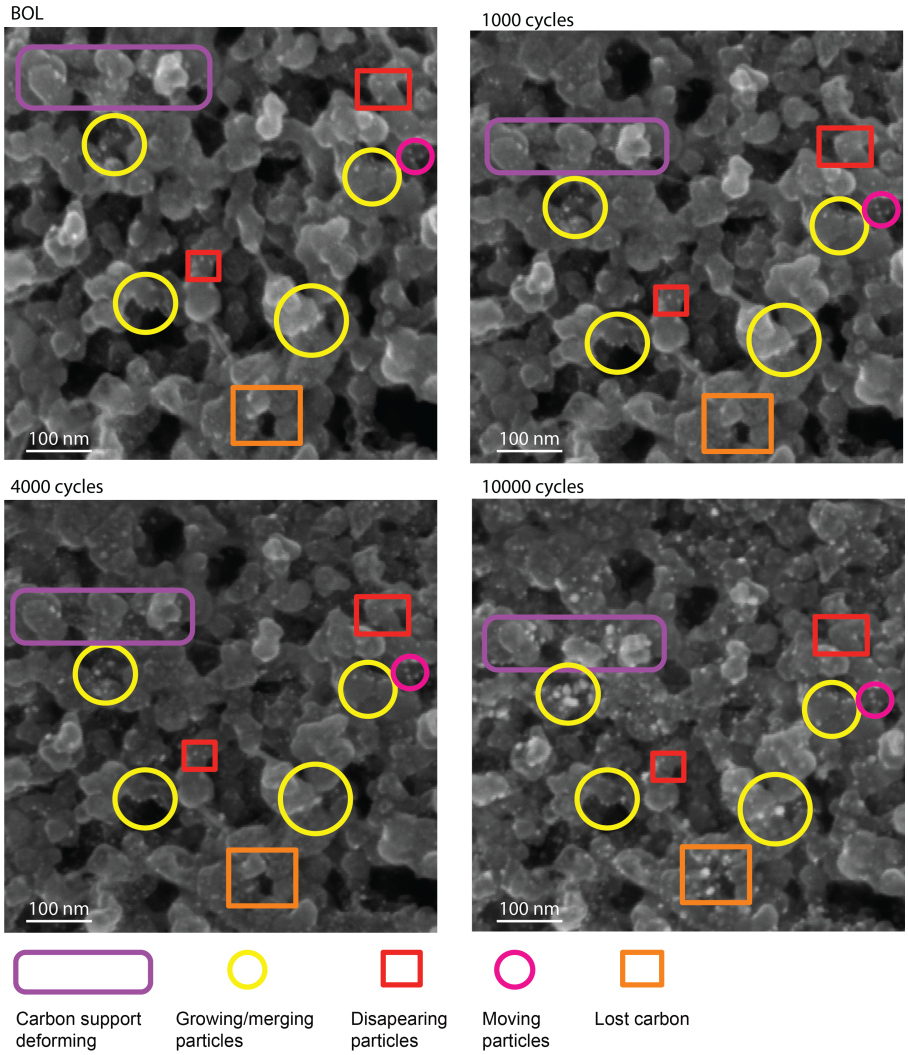

Figure 5.7: High magnification SEM images at BOL and after 1000, 4000 and 10 000 normal condition AST cycles. Some degradation effects have been marked with circles and rectangles as a guide for the reader. The markings are not comprehensive.

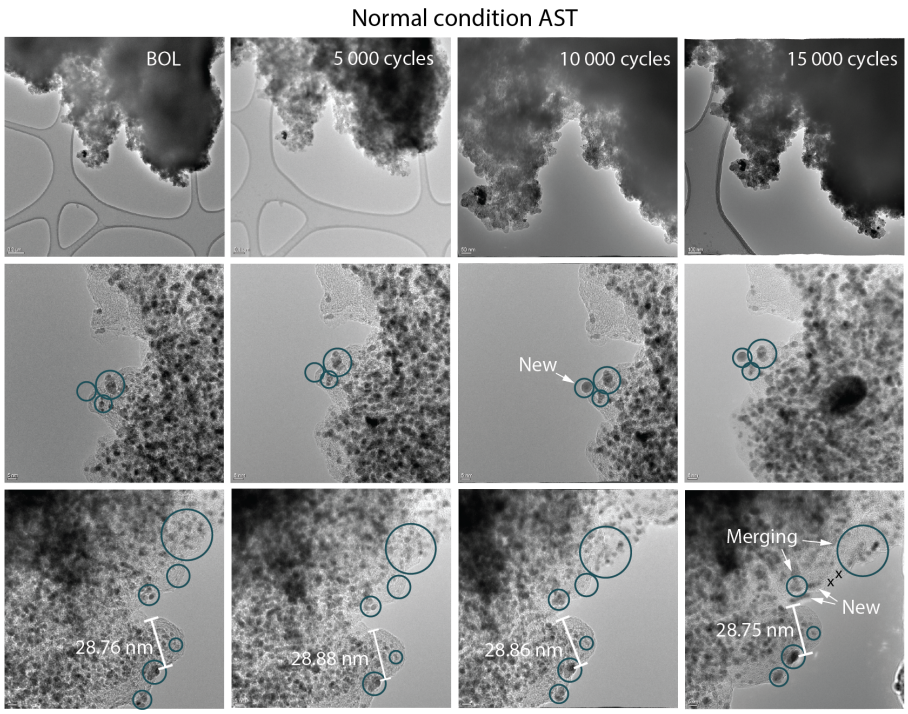

Figure 5.8: IL-TEM images at BOL and after 5000, 10 000 and 15 000 normal condition AST cycles.

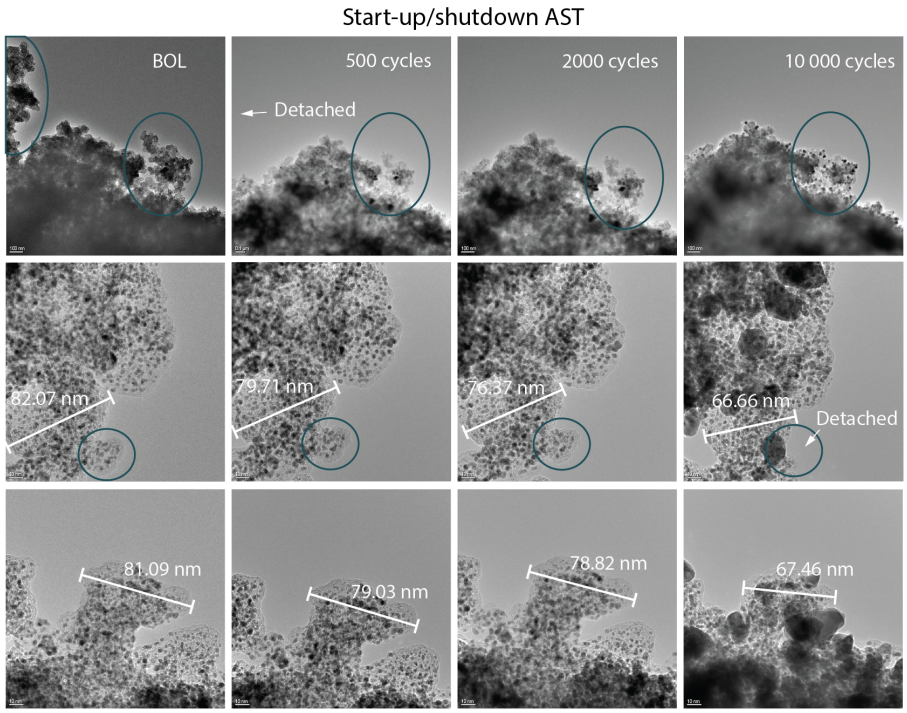

Figure 5.9: IL-TEM images at BOL and after 500, 2000 and 10 000 start-up/shutdown AST cycles.

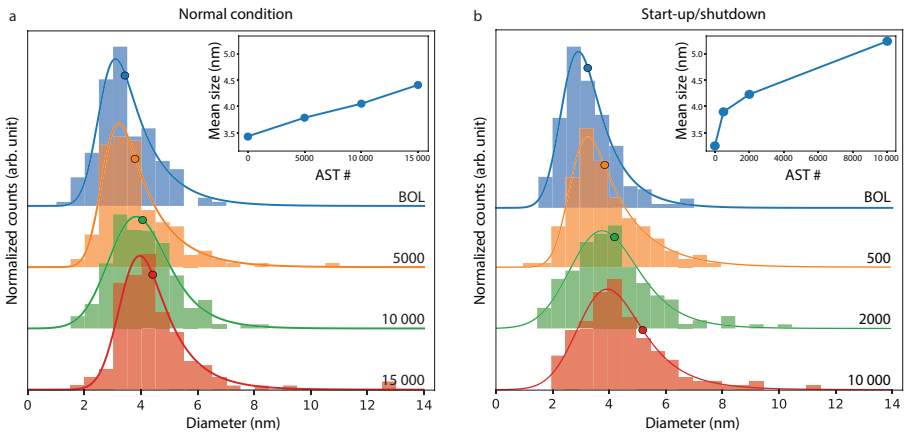

Figure 5.10: Particle size distribution calculated from IL-TEM images after each AST session for a) normal condition AST and b) start-up/shutdown AST. Inset shows mean size. The x-axis of the histogram for the start-up/shutdown AST have been limited to 14 nm, even though particle up to 30 nm could be seen at the EOL. The mean size was calculated using the full set of measured particles.

by the IL-TEM imaging must take place.

The much more rapid decline in performance during start-up/shutdown AST (Fig. 5.4b) can be partly explained by the degradation of the carbon support. The degradation of the carbon support has several effects. Firstly, collapse of the carbon support might lead to detachment between membrane, the CL and the GDL, leading to higher contact resistance. Moreover, loss of support for the Pt particles means they are more likely to detach, and maybe reattach on locations without sufficient electrical contact or without ionomer for proton conductivity. All these effects together can explain the large increase of HFR seen in Fig. 5.4b. Furthermore, the collapse of the porous carbon support structure might lead to increased mass transport resistance of reactants. The combined effect of higher cell resistance and mass transport limitations can explain the large loss of performance in Fig. 5.4b.

Chapter 6

Conclusions & Outlook

Fuel cells, and in particular proton exchange membrane fuel cells (PEMFCs), are expected to be important for the decarbonisation of the energy and transport sectors. However, PEMFC suffers issues related to degradation. To design more durable materials and better mitigation strategies, the degradation mechanisms of the different PEMFC components have to be better understood.

By combining identical location (IL) scanning electron microscopy (SEM) and IL transmission electron microscopy (TEM) imaging with single cell fuel cell measurements, we have managed to follow the degradation of the cathodic catalytic layer (CL) of a PEMFC under real operation conditions, which have not been done before. We have demonstrated that it is possible to open up the fuel cell, disassemble the membrane electrode assembly and image the CL in vacuum, without harming the fuel cell performance or changing the electrochemical characteristics. So far, we have used these methods to study the degradation of the CL during two different types of accelerated stress tests (ASTs). One focusing on degradation during normal operation condition, and one mimicking degradation during start-up/shutdown events. We showed that the CL degrades by different mechanisms during respective AST. In particular, we showed that during start-up/shutdown conditions, the carbon support looses volume, which brings Pt particles physically closer to each-other, which in turn promotes Pt agglomeration, coalescence and particle growth. This has not been previously observed. Overall, these results demonstrate the possibility of performing IL electron microscopy under realistic fuel cell conditions, and the strength of combining macro- and nanoscale imaging with electrochemical analysis. Even so, the methods are not perfect, and have room for improvements. One issue is the fact that we only observe the top of the catalyst layer farthest from the membrane, and the degradation is known to differ throughout the cross section of the CL. Optimally, similar measurements would be performed while looking at the degradation at different depths in the CL/MEA. However, due to how the MEA is constructed, it is hard to image the CL closer to the membrane without permanently damaging the sample, which would make the repeated testing needed for IL imaging troublesome. Furthermore, the introduction of TEM grids into the MEA does change the

local environment by introducing different materials in form of the Au grid, and can change the local transportation of gases. This could affect the results, and should be kept in mind. However, the same could certainly be said for IL imaging done in liquid electrolyte, and the results presented here should give an indication of how degradation in PEMFC environments transpire compared to previous liquid half cell testing. The effects of TEM grids on the local environment, and how that potentially affects the degradation of the sample should be investigated further, to gain an even better understanding of the true degradation processes transpiring inside the PEMFC CL.

Furthermore we have studied the behaviour of Pt thin films in acidic and alkaline environments using electrochemical quarts crystal micro-balance. The Pt thin films gains more mass during oxidation in alkaline as compared to acidic environments, and the point of minimum mass is located at a higher potential in alkaline electrolyte, which coincides with the differences in CVs in either electrolyte. Furthermore, Pt starts to dissolve noticeably when the potential is cycled to above 1.1 V both in 1 M KOH and 0.5 M H_2SO_4, and the dissolution rates are similar in either electrolyte despite the difference in oxide formation.

For future work, I would like to continue develop the IL techniques presented in this thesis, to delve further into the degradation mechanisms in real fuel cell conditions, and possibly investigate how such behaviour differs between real fuel cell set-ups and model systems. In particular, it would be of interest to study degradation behaviour of PEMFCs under higher temperatures, since effort is currently being made to develop intermediate temperature PEMFCs. Ultimately, I would like to use these methods to study the degradation of more novel catalyst materials in real PEMFC conditions, to see how their stability compares to that of the industry standard Pt.

Acknowledgment

This work is financially supported by the the Sweden Foundation for Strategic Research (Stiftelsen för strategisk forskning, SSF).

First, I would like to thank my supervisor Björn Wickman, for giving me the opportunity to pursue this licentiate, and supporting me throughout it, and my examiner Henrik Grönbeck.

I would also like to thank the members of the electrochemistry group, for all the guidance and help they have offered me, and for creating a great and relaxing working environment. Especially I would like to thank Victor Shokhen, for teaching me and encouraging me throughout my licentiate, and not least at all for helping me create some wonderful illustrations for this thesis.

I would deeply like to thank my friends, acquaintances, fellow musicians and scout leaders for keeping me sane, and reminding me that there indeed is a world outside of academia.

Last but not least, I would like to thank my family, for being there for me at all times, in good times and bad. Especially to my brothers, for inspiring and motivating me to be a better me, and whom without I most likely would not have tried pursuing a PhD in the first place.

You all have had a role in bringing me to where I am today,
Thank you all, truly.

Bibliography

[1] M. Kappelle *et al.*, *WMO Statement on the State of the Global Climate in 2019*, 2020.

[2] UNFCCC, "Paris agreement," in *Report of the Conference of the Parties to the United Nations Framework Convention on Climate Change (21st Session, 2015: Paris)*, vol. 4, 2015, p. 2017.

[3] NOAA National Centers for Environmental information. "Climate at a glance: Global time series." (2022), [Online]. Available: https://www.ncdc.noaa.gov/cag/ (visited on 20/10/2022).

[4] P. Friedlingstein *et al.*, "Global carbon budget 2021," *Earth System Science Data*, vol. 14, no. 4, pp. 1917–2005, 2022.

[5] United Nations, "Transforming our world: The 2030 agenda for sustainable development," *New York: United Nations, Department of Economic and Social Affairs*, 2015.

[6] Energimyndigheten. "Sverige har överträffat målet om andel förnybar energi för 2020." (2022), [Online]. Available: https://www.energimyndigheten.se/nyhetsarkiv/2022/sverige-har-overtraffat-malet-om-andel-fornybar-energi-for-2020/ (visited on 05/10/2022).

[7] Statistikmyndigheten SCB. "Elproduktion och förbrukning i Sverige." (2022), [Online]. Available: https://www.scb.se/hitta-statistik/sverige-i-siffror/miljo/elektricitet-i-sverige/ (visited on 05/10/2022).

[8] Energiföretagen Sverige. "Elproduktion." (2018), [Online]. Available: https://www.energiforetagen.se/energifakta/elsystemet/produktion/#:~:text=Den\%20el\%20som\%20produceras\%20i,kraftslagen\%20som\%20sol\%20och\%20vind. (visited on 05/10/2022).

[9] H. Ritchie, M. Roser and P. Rosado, "CO_2 and Greenhouse Gas Emissions," *Our World in Data*, 2020, https://ourworldindata.org/co2-and-other-greenhouse-gas-emissions.

[10] X. Zeng *et al.*, "Commercialization of lithium battery technologies for electric vehicles," *Advanced Energy Materials*, vol. 9, no. 27, p. 1 900 161, 2019.

[11] K. Forrest, M. Mac Kinnon, B. Tarroja and S. Samuelsen, "Estimating the technical feasibility of fuel cell and battery electric vehicles for the medium and heavy duty sectors in california," *Applied Energy*, vol. 276, p. 115 439, 2020.

[12] N. Gray, S. McDonagh, R. O'Shea, B. Smyth and J. D. Murphy, "Decarbonising ships, planes and trucks: An analysis of suitable low-carbon fuels for the maritime, aviation and haulage sectors," *Advances in Applied Energy*, vol. 1, p. 100 008, 2021.

[13] Office of Fossil Energy, United States Department of Energy. "Hydrogen Strategy, Enabling a Low-Carbon Economy." (2020), [Online]. Available: `chrome-extension://efaidnbmnnnibpcajpcglclefindmkaj/https://www.energy.gov/sites/prod/files/2020/07/f76/USDOE_FE_Hydrogen_Strategy_July2020.pdf` (visited on 03/11/2022).

[14] D. R. Palo, R. A. Dagle and J. D. Holladay, "Methanol steam reforming for hydrogen production," *Chemical reviews*, vol. 107, no. 10, pp. 3992–4021, 2007.

[15] Z. Abdin, A. Zafaranloo, A. Rafiee, W. Mérida, W. Lipiński and K. R. Khalilpour, "Hydrogen as an energy vector," *Renewable and sustainable energy reviews*, vol. 120, p. 109 620, 2020.

[16] T. K. Mandal and D. H. Gregory, "Hydrogen: A future energy vector for sustainable development," *Proceedings of the institution of mechanical engineers, part C: journal of mechanical engineering science*, vol. 224, no. 3, pp. 539–558, 2010.

[17] Í. Martín-García, E. Rosales-Asensio, A. González-Martínez, S. Bracco, F. Delfino and M. de Simón-Martín, "Hydrogen as an energy vector to optimize the energy exploitation of a self-consumption solar photovoltaic facility in a dwelling house," *Energy Reports*, vol. 6, pp. 155–166, 2020.

[18] Wikipedia. "Energy density." (2022), [Online]. Available: `https://en.wikipedia.org/wiki/Energy_density` (visited on 20/10/2022).

[19] D. Papageorgopoulos, "Fuel Cell RD Overview 2019 Annual Merit Review and Peer Evaluation Meeting," U.S. Department of Energy, Salt Lake City, UT, Tech. Rep., 2019.

[20] A. Wilson, G. Kleen and D. Papageorgopoulos, *Fuel Cell System Cost - 2017*. Department of Energy, 2017.

[21] United States Department of Energy, "Fuel Cell Technical Team Roadmap," Jun. 2013. DOI: `10.2172/1220127`. [Online]. Available: `https://www.osti.gov/biblio/1220127`.

[22] Clean Hydrogen Joint Undertaking, "Clean Hydrogen joint undertaking (Clean Hydrogen JU) work programme 2022," 2022.

[23] J. Niemantsverdriet and I Chorkendorff, *Concepts of modern catalysis and kinetics*. John Wiley & Sons, 2006.

[24] S. Ghosh, "Fertiliser Technology: Fractured Profile of Self-Reliance," *Economic and Political Weekly*, pp. 698–705, 1986.

[25] F. H. Blanding, "Reaction rates in catalytic cracking of petroleum," *Industrial & Engineering Chemistry*, vol. 45, no. 6, pp. 1186–1197, 1953.

[26] N. Corrigan, S. Shanmugam, J. Xu and C. Boyer, "Photocatalysis in organic and polymer synthesis," *Chemical Society Reviews*, vol. 45, no. 22, pp. 6165–6212, 2016.

[27] J. P. Lutz, M. D. Hannigan and A. J. McNeil, "Polymers synthesized via catalyst-transfer polymerization and their applications," *Coordination Chemistry Reviews*, vol. 376, pp. 225–247, 2018.

[28] J. R. Rostrup-Nielsen, "Catalytic steam reforming," in *Catalysis*, Springer, 1984, pp. 1–117.

[29] S. Sá, H. Silva, L. Brandão, J. M. Sousa and A. Mendes, "Catalysts for methanol steam reforming–A review," *Applied Catalysis B: Environmental*, vol. 99, no. 1-2, pp. 43–57, 2010.

[30] J. Li, X. Meng and F.-S. Xiao, "Zeolites for control of NOx emissions: Opportunities and challenges," *Chem Catalysis*, 2021.

[31] L. Zhang *et al.*, "Recent advances in the preparation of zeolites for the selective catalytic reduction of NOx in diesel engines," *Reaction Chemistry & Engineering*, vol. 4, no. 6, pp. 975–985, 2019.

[32] J. Wang, H. Chen, Z. Hu, M. Yao and Y. Li, "A review on the Pd-based three-way catalyst," *Catalysis Reviews*, vol. 57, no. 1, pp. 79–144, 2015.

[33] S. Rood, S. Eslava, A. Manigrasso and C. Bannister, "Recent advances in gasoline three-way catalyst formulation: A review," *Proceedings of the Institution of Mechanical Engineers, Part D: Journal of Automobile Engineering*, vol. 234, no. 4, pp. 936–949, 2020.

[34] H. Ooka, J. Huang and K. S. Exner, "The Sabatier principle in electrocatalysis: Basics, limitations, and extensions," *Frontiers in Energy Research*, vol. 9, p. 654 460, 2021.

[35] J. K. Nørskov *et al.*, "Origin of the overpotential for oxygen reduction at a fuel-cell cathode," *The Journal of Physical Chemistry B*, vol. 108, no. 46, pp. 17 886–17 892, 2004.

[36] E. Whittaker, *A History of the Theories of Aether and Electricity: Vol. I: The Classical Theories; Vol. II: The Modern Theories, 1900-1926*. Courier Dover Publications, 1989, vol. 1.

[37] A. Volta and J. Banks, "I. On the electricity excited by the mere contact of conducting substances of different kinds," *The Philosophical Magazine*, vol. 7, no. 28, pp. 289–311, 1800.

[38] E. Fabbri and T. J. Schmidt, *Oxygen evolution reaction—the enigma in water electrolysis*, 2018.

[39] W. R. Grove, "LVI. On a new voltaic combination: To the editors of the Philosophical Magazine and Journal," *The London, Edinburgh, and Dublin Philosophical Magazine and Journal of Science*, vol. 13, no. 84, pp. 430–431, 1838.

[40] Cambridge Independent. "Apollo 11 mission 50 years on: The Cambridge scientist who helped put man on the moon." (2019), [Online]. Available: https://www.cambridgeindependent.co.uk/news/apollo-11-mission-50-years-on-the-cambridge-scientist-who-helped-put-man-on-the-moon-9077166/ (visited on 10/10/2022).

[41] E. J. Dickinson and A. J. Wain, "The butler-volmer equation in electrochemical theory: Origins, value, and practical application," *Journal of Electroanalytical Chemistry*, vol. 872, p. 114 145, 2020.

[42] M. Pourbaix, *ATLAS OF ELECTROCHEMICAL EQUILIBRIA IN AQUEOUS SOLUTIONS*. National Association of Corrosion Engineers, 1974.

[43] R. M. Ormerod, "Solid oxide fuel cells," *Chemical Society Reviews*, vol. 32, no. 1, pp. 17–28, 2003.

[44] H. A. Gasteiger, S. S. Kocha, B. Sompalli and F. T. Wagner, "Activity benchmarks and requirements for Pt, Pt-alloy, and non-Pt oxygen reduction catalysts for PEMFCs," *Applied Catalysis B: Environmental*, vol. 56, no. 1-2, pp. 9–35, 2005.

[45] Z. Xu, H. Zhang, H. Zhong, Q. Lu, Y. Wang and D. Su, "Effect of particle size on the activity and durability of the Pt/C electrocatalyst for proton exchange membrane fuel cells," *Applied Catalysis B: Environmental*, vol. 111, pp. 264–270, 2012.

[46] D. Y. Chung, J. M. Yoo and Y.-E. Sung, "Highly durable and active pt-based nanoscale design for fuel-cell oxygen-reduction electrocatalysts," *Advanced materials*, vol. 30, no. 42, p. 1 704 123, 2018.

[47] "Carbon Black - Ketjenblack EC-600JD." (2022), [Online]. Available: https://www.fuelcellstore.com/ketjenblack-carbon-black-ec600jd (visited on 01/11/2022).

[48] G.-F. Li, D. Yang and P.-Y. Abel Chuang, "Defining nafion ionomer roles for enhancing alkaline oxygen evolution electrocatalysis," *ACS Catalysis*, vol. 8, no. 12, pp. 11 688–11 698, 2018.

[49] K. Shinozaki, Y. Morimoto, B. S. Pivovar and S. S. Kocha, "Suppression of oxygen reduction reaction activity on pt-based electrocatalysts from ionomer incorporation," *Journal of Power Sources*, vol. 325, pp. 745–751, 2016.

[50] K. Jiao *et al.*, "Designing the next generation of proton-exchange membrane fuel cells," *Nature*, vol. 595, no. 7867, pp. 361–369, 2021.

[51] I. E. Stephens, A. S. Bondarenko, L. Bech and I. Chorkendorff, "Oxygen electroreduction activity and x-ray photoelectron spectroscopy of platinum and early transition metal alloys," *ChemCatChem*, vol. 4, no. 3, pp. 341–349, 2012.

[52] M. Escudero-Escribano *et al.*, "Tuning the activity of Pt alloy electrocatalysts by means of the lanthanide contraction," *Science*, vol. 352, no. 6281, pp. 73–76, 2016.

[53] M. Escudero-Escribano *et al.*, "Pt5Gd as a highly active and stable catalyst for oxygen electroreduction," *Journal of the American Chemical Society*, vol. 134, no. 40, pp. 16 476–16 479, 2012.

[54] J Greeley *et al.*, "Alloys of platinum and early transition metals as oxygen reduction electrocatalysts," *Nature chemistry*, vol. 1, no. 7, pp. 552–556, 2009.

[55] V. R. Stamenkovic *et al.*, "Improved oxygen reduction activity on Pt3Ni (111) via increased surface site availability," *science*, vol. 315, no. 5811, pp. 493–497, 2007.

[56] F. Zhou, Y. Yan, S. Guan, W. Guo, M. Sun and M. Pan, "Solving Nafion poisoning of ORR catalysts with an accessible layer: designing a nanostructured core-shell Pt/C catalyst via a one-step self-assembly for PEMFC," *International Journal of Energy Research*, vol. 44, no. 13, pp. 10 155–10 167, 2020.

[57] K. Wang *et al.*, "Iron oxide@ graphitic carbon core-shell nanoparticles embedded in ordered mesoporous N-doped carbon matrix as an efficient cathode catalyst for PEMFC," *Applied Catalysis B: Environmental*, vol. 264, p. 118 468, 2020.

[58] C. Chen *et al.*, "Highly crystalline multimetallic nanoframes with three-dimensional electrocatalytic surfaces," *Science*, vol. 343, no. 6177, pp. 1339–1343, 2014.

[59] F. Xiao *et al.*, "Recent advances in electrocatalysts for proton exchange membrane fuel cells and alkaline membrane fuel cells," *Advanced Materials*, vol. 33, no. 50, p. 2 006 292, 2021.

[60] S. J. Hamrock and M. A. Yandrasits, "Proton exchange membranes for fuel cell applications," *Journal of Macromolecular Science, Part C: Polymer Reviews*, vol. 46, no. 3, pp. 219–244, 2006.

[61] V. Vishnyakov, "Proton exchange membrane fuel cells," *Vacuum*, vol. 80, no. 10, pp. 1053–1065, 2006.

[62] W. Grot, *Fluorinated ionomers*. William Andrew, 2011.

[63] T. A. Zawodzinski *et al.*, "Water uptake by and transport through Nafion® 117 membranes," *Journal of the electrochemical society*, vol. 140, no. 4, p. 1041, 1993.

[64] M. K. Petersen and G. A. Voth, "Characterization of the solvation and transport of the hydrated proton in the perfluorosulfonic acid membrane Nafion," *The Journal of Physical Chemistry B*, vol. 110, no. 37, pp. 18 594–18 600, 2006.

[65] C Yang, P Costamagna, S Srinivasan, J Benziger and A. B. Bocarsly, "Approaches and technical challenges to high temperature operation of proton exchange membrane fuel cells," *Journal of Power Sources*, vol. 103, no. 1, pp. 1–9, 2001.

[66] C. Schmidt, T. Glück and G. Schmidt-Naake, "Modification of Nafion membranes by impregnation with ionic liquids," *Chemical Engineering & Technology: Industrial Chemistry-Plant Equipment-Process Engineering-Biotechnology*, vol. 31, no. 1, pp. 13–22, 2008.

[67] A. Sahu, S Pitchumani, P Sridhar and A. Shukla, "Nafion and modified-Nafion membranes for polymer electrolyte fuel cells: An overview," *Bulletin of Materials Science*, vol. 32, no. 3, pp. 285–294, 2009.

[68] A. Chandan *et al.*, "High temperature (HT) polymer electrolyte membrane fuel cells (PEMFC)–A review," *Journal of Power Sources*, vol. 231, pp. 264–278, 2013.

[69] R. Rosli *et al.*, "A review of high-temperature proton exchange membrane fuel cell (HT-PEMFC) system," *International Journal of Hydrogen Energy*, vol. 42, no. 14, pp. 9293–9314, 2017.

[70] H.-Y. Jung and J. W. Kim, "Role of the glass transition temperature of Nafion 117 membrane in the preparation of the membrane electrode assembly in a direct methanol fuel cell (DMFC)," *International Journal of Hydrogen Energy*, vol. 37, no. 17, pp. 12 580–12 585, 2012.

[71] S. J. Osborn, M. K. Hassan, G. M. Divoux, D. W. Rhoades, K. A. Mauritz and R. B. Moore, "Glass transition temperature of perfluorosulfonic acid ionomers," *Macromolecules*, vol. 40, no. 10, pp. 3886–3890, 2007.

[72] K. D. Baik, B. K. Hong and M. S. Kim, "Effects of operating parameters on hydrogen crossover rate through Nafion® membranes in polymer electrolyte membrane fuel cells," *Renewable Energy*, vol. 57, pp. 234–239, 2013.

[73] C. Francia, V. S. Ijeri, S. Specchia and P. Spinelli, "Estimation of hydrogen crossover through Nafion® membranes in PEMFCs," *Journal of Power Sources*, vol. 196, no. 4, pp. 1833–1839, 2011.

[74] L Cindrella *et al.*, "Gas diffusion layer for proton exchange membrane fuel cells—A review," *Journal of Power Sources*, vol. 194, no. 1, pp. 146–160, 2009.

[75] G. Kaur, *PEM Fuel Cells: Fundamentals, Advanced Technologies, and Practical Application*. Elsevier, 2021.

[76] F Basile, A Barbir and T. Veziroglu, *Compendium of Hydrogen Energy, Volume 3: Hydrogen Energy Conversion*. Elsevier, Woodgead Publishing, 2016.

[77] R. G. Akay and A. B. Yurtcan, *Direct Liquid Fuel Cells: Fundamentals, Advances and Future*. Academic Press, 2020.

[78] X. Li and I. Sabir, "Review of bipolar plates in pem fuel cells: Flow-field designs," *International journal of hydrogen energy*, vol. 30, no. 4, pp. 359–371, 2005.

[79] H. Kahraman and M. F. Orhan, "Flow field bipolar plates in a proton exchange membrane fuel cell: Analysis & modeling," *Energy Conversion and Management*, vol. 133, pp. 363–384, 2017.

[80] J Scholta, B Rohland, V Trapp and U Focken, "Investigations on novel low-cost graphite composite bipolar plates," *Journal of Power Sources*, vol. 84, no. 2, pp. 231–234, 1999.

[81] S. Kim and I. Hong, "Effects of humidity and temperature on a proton exchange membrane fuel cell (pemfc) stack," *Journal of Industrial and Engineering Chemistry*, vol. 14, no. 3, pp. 357–364, 2008.

[82] K. Neyerlin, H. A. Gasteiger, C. K. Mittelsteadt, J. Jorne and W. Gu, "Effect of relative humidity on oxygen reduction kinetics in a pemfc," *Journal of The Electrochemical Society*, vol. 152, no. 6, A1073, 2005.

[83] Y. H. Park and J. A. Caton, "An experimental investigation of electro-osmotic drag coefficients in a polymer electrolyte membrane fuel cell," *International Journal of Hydrogen Energy*, vol. 33, no. 24, pp. 7513–7520, 2008.

[84] U. Basuli *et al.*, "Properties and degradation of the gasket component of a proton exchange membrane fuel cell—a review," *Journal of Nanoscience and Nanotechnology*, vol. 12, no. 10, pp. 7641–7657, 2012.

[85] S Asghari, M. Shahsamandi and M. A. Khorasani, "Design and manufacturing of end plates of a 5 kw pem fuel cell," *International journal of hydrogen energy*, vol. 35, no. 17, pp. 9291–9297, 2010.

[86] Y.-J. Sohn *et al.*, "Operating characteristics of an air-cooling pemfc for portable applications," *Journal of Power Sources*, vol. 145, no. 2, pp. 604–609, 2005.

[87] M. H. Bargal, M. A. Abdelkareem, Q. Tao, J. Li, J. Shi and Y. Wang, "Liquid cooling techniques in proton exchange membrane fuel cell stacks: A detailed survey," *Alexandria Engineering Journal*, vol. 59, no. 2, pp. 635–655, 2020.

[88] R. Adžić, *Recent advances in the kinetics of oxygen reduction*. Wiley-VCH, New York, 1998, vol. 197.

[89] X. Wang *et al.*, "Review of metal catalysts for oxygen reduction reaction: From nanoscale engineering to atomic design," *Chem*, vol. 5, no. 6, pp. 1486–1511, 2019.

[90] A. R. Kucernak and C. Zalitis, "General models for the electrochemical hydrogen oxidation and hydrogen evolution reactions: Theoretical derivation and experimental results under near mass-transport free conditions," *The Journal of Physical Chemistry C*, vol. 120, no. 20, pp. 10 721–10 745, 2016.

[91] M. K. Debe, "Electrocatalyst approaches and challenges for automotive fuel cells," *Nature*, vol. 486, no. 7401, pp. 43–51, 2012.

[92] L. Zhang *et al.*, "Ti_4O_7 supported Ru@Pt core–shell catalyst for CO-tolerance in PEM fuel cell hydrogen oxidation reaction," *Applied energy*, vol. 103, pp. 507–513, 2013.

[93] F Bortoloti, A. Garcia and A. Angelo, "Electronic effect in intermetallic electrocatalysts with low susceptibility to CO poisoning during hydrogen oxidation," *international journal of hydrogen energy*, vol. 40, no. 34, pp. 10 816–10 824, 2015.

[94] S. Lee, S Mukerjee, E. Ticianelli and J McBreen, "Electrocatalysis of CO tolerance in hydrogen oxidation reaction in PEM fuel cells," *Electrochimica Acta*, vol. 44, no. 19, pp. 3283–3293, 1999.

[95] W. M. Haynes, D. R. Lide and T. J. Bruno, *CRC handbook of chemistry and physics*. CRC press, 2016.

[96] S.Bhattacharjee, *Molar enthalpy of formation of various substances*. [Online]. Available: `https://www.ohio.edu/mechanical/thermo/property_tables/combustion/Enth_Formation.html` (visited on 01/11/2022).

[97] S. A. Vilekar and R. Datta, "The effect of hydrogen crossover on open-circuit voltage in polymer electrolyte membrane fuel cells," *Journal of Power Sources*, vol. 195, no. 8, pp. 2241–2247, 2010.

[98] A. A. Topalov *et al.*, "Dissolution of platinum: Limits for the deployment of electrochemical energy conversion?" *Angewandte Chemie International Edition*, vol. 51, no. 50, pp. 12 613–12 615, 2012.

[99] C. A. Reiser *et al.*, "A reverse-current decay mechanism for fuel cells," *Electrochemical and Solid-State Letters*, vol. 8, no. 6, A273, 2005.

[100] K. Kinoshita, "Carbon: Electrochemical and physicochemical properties," 1988.

[101] L. Roen, C. Paik and T. Jarvi, "Electrocatalytic corrosion of carbon support in PEMFC cathodes," *Electrochemical and solid-state letters*, vol. 7, no. 1, A19, 2003.

[102] A. Perego *et al.*, "Investigation of cathode catalyst layer interfaces evolution during accelerated stress tests for polymer electrolyte fuel cells," *Applied Catalysis B: Environmental*, vol. 301, p. 120 810, 2022.

[103] Y. Luo and K. Jiao, "Cold start of proton exchange membrane fuel cell," *Progress in Energy and Combustion Science*, vol. 64, pp. 29–61, 2018.

[104] R. Mukundan *et al.*, *V.D.3 Accelerated Testing Validation*. United States Department of Energy, 2013.

[105] B.-T. Huang *et al.*, "Experimental investigation of air relative humidity (RH) cycling tests on MEA/cell aging in PEMFC part I: study of high RH cycling test with air RH at 62%/100%," *Fuel Cells*, vol. 12, no. 3, pp. 335–346, 2012.

[106] S. Cherevko, G. P. Keeley, N. Kulyk and K. J. Mayrhofer, "Pt submonolayer on Au: System stability and insights into platinum electrochemical dissolution," *Journal of The Electrochemical Society*, vol. 163, no. 3, H228, 2016.

[107] G. Sauerbrey, "Verwendung von schwingquarzen zur wägung dünner schichten und zur mikrowägung," *Zeitschrift für physik*, vol. 155, no. 2, pp. 206–222, 1959.

[108] W. Sheng, Z. Zhuang, M. Gao, J. Zheng, J. G. Chen and Y. Yan, "Correlating hydrogen oxidation and evolution activity on platinum at different ph with measured hydrogen binding energy," *Nature communications*, vol. 6, no. 1, pp. 1–6, 2015.

[109] G. Karlberg, T. Jaramillo, E. Skulason, J. Rossmeisl, T. Bligaard and J. K. Nørskov, "Cyclic voltammograms for H on Pt (111) and Pt (100) from first principles," *Physical review letters*, vol. 99, no. 12, p. 126 101, 2007.

[110] T Biegler, D. Rand and R Woods, "Limiting oxygen coverage on platinized platinum; relevance to determination of real platinum area by hydrogen adsorption," *Journal of Electroanalytical Chemistry and Interfacial Electrochemistry*, vol. 29, no. 2, pp. 269–277, 1971.

[111] S. Brummer, "The use of large anodic galvanostatic transients to evaluate the maximum adsorption on platinum from formic acid solutions," *The Journal of Physical Chemistry*, vol. 69, no. 2, pp. 562–571, 1965.

[112] S. Stariha *et al.*, "Recent advances in catalyst accelerated stress tests for polymer electrolyte membrane fuel cells," *Journal of The Electrochemical Society*, vol. 165, no. 7, F492, 2018.

[113] G. Tsotridis, A. Pilenga, G. De Marco, T. Malkow *et al.*, "EU harmonised test protocols for PEMFC MEA testing in single cell configuration for automotive applications," *JRC Science for Policy report*, vol. 27632, 2015.

[114] US DRIVE Fuel Cell TechTeam, "Appendix A: FCTT AST and polarization curve protocols for PEMFCs," *US Department of Energy*,

[115] R. Mukundan *et al.*, "Vh 5 accelerated testing validation," *Target*, vol. 40, no. 12,600, pp. 22–200,

[116] G. Jerkiewicz, G. Vatankhah, S.-i. Tanaka and J. Lessard, "Discovery of the potential of minimum mass for platinum electrodes," *Langmuir*, vol. 27, no. 7, pp. 4220–4226, 2011.

[117] N Macauley *et al.*, "Pt band formation enhances the stability of fuel cell membranes," *ECS Electrochemistry Letters*, vol. 2, no. 4, F33, 2013.